Prepared for submission to JCAP

The large scale polarization explorer (LSPE) for CMB measurements: performance forecast

The LSPE collaboration

G. Addamo,[a] **P. A. R. Ade,**[b] **C. Baccigalupi,**[c] **A. M. Baldini,**[d] **P. M. Battaglia,**[e] **E. S. Battistelli,**[f,g] **A. Baù,**[h] **P. de Bernardis,**[f,g] **M. Bersanelli,**[i,j] **M. Biasotti,**[k,l] **A. Boscaleri,**[m] **B. Caccianiga,**[j] **S. Caprioli,**[i,j] **F. Cavaliere,**[i,j] **F. Cei,**[f,n] **K. A. Cleary,**[o] **F. Columbro,**[f,g] **G. Coppi,**[p] **A. Coppolecchia,**[f,g] **F. Cuttaia,**[q] **G. D'Alessandro,**[f,g] **G. De Gasperis,**[r,s] **M. De Petris,**[f,g] **V. Fafone,**[r,s] **F. Farsian,**[c] **L. Ferrari Barusso,**[k,l] **F. Fontanelli,**[k,l] **C. Franceschet,**[i,j] **T.C. Gaier,**[u] **L. Galli,**[d] **F. Gatti,**[k,l] **R. Genova-Santos,**[t,v] **M. Gerbino,**[D,C] **M. Gervasi,**[h,w] **T. Ghigna,**[x] **D. Grosso,**[k,l] **A. Gruppuso,**[q,H] **R. Gualtieri,**[G] **F. Incardona,**[i,j] **M. E. Jones,**[x] **P. Kangaslahti,**[o] **N. Krachmalnicoff,**[c] **L. Lamagna,**[f,g] **M. Lattanzi,**[D,C] **M. Lumia,**[a] **R. Mainini,**[h] **D. Maino,**[i,j] **S. Mandelli,**[i,j] **M. Maris,**[y] **S. Masi,**[f,g] **S. Matarrese,**[z] **A. May,**[A] **L. Mele,**[f,g] **P. Mena,**[B] **A. Mennella,**[i,j] **R. Molina,**[B] **D. Molinari,**[q,E,C,D] **G. Morgante,**[q] **U. Natale,**[C,D] **F. Nati,**[h] **P. Natoli,**[C,D] **L. Pagano,**[C,D] **A. Paiella,**[f,g] **F. Panico,**[f] **F. Paonessa,**[a] **S. Paradiso,**[i,j] **A. Passerini,**[h] **M. Perez-de-Taoro,**[t] **O. A. Peverini,**[a] **F. Pezzotta,**[i,j] **F. Piacentini,**[f,g,1] **L. Piccirillo,**[A] **G. Pisano,**[b] **G. Polenta,**[F] **D. Poletti,**[c] **G. Presta,**[f,g] **S. Realini,**[i,j] **N. Reyes,**[B] **A. Rocchi,**[r,s] **J. A. Rubino-Martin,**[t,v] **M. Sandri,**[q] **S. Sartor,**[y] **A. Schillaci,**[o] **G. Signorelli,**[d] **B. Siri,**[k,l] **M. Soria,**[o] **F. Spinella,**[d] **V. Tapia,**[B] **A. Tartari,**[d] **A. C. Taylor,**[x] **L. Terenzi,**[q] **M. Tomasi,**[i,j] **E. Tommasi,**[F] **C. Tucker,**[b] **D. Vaccaro,**[d] **D. M. Vigano,**[i,j] **F. Villa,**[q] **G. Virone,**[a] **N. Vittorio,**[r,s] **A. Volpe,**[F] **R. E. J. Watkins,**[x] **A. Zacchei,**[y] **M. Zannoni**[h,w]

[a]CNR–IEIIT, Corso Duca degli Abruzzi, 24, 10129 Torino TO, Italy

[b]School of Physics and Astronomy, Cardiff University, Queens Buildings, The Parade, Cardiff, CF24 3AA, U.K.

[1]Corresponding author

[c]SISSA, Astrophysics Sector, via Bonomea 265, 34136, Trieste, Italy
[d]INFN–Sezione di Pisa, Largo B. Pontecorvo 3, 56127 Pisa (Italy)
[e]INAF/IASF Milano, Via E. Bassini 15, Milano, Italy
[f]Dipartimento di Fisica, Sapienza Università di Roma, P.le A. Moro 5, 00185, Roma, Italy
[g]INFN–Sezione di Roma1, P.le A. Moro 5, 00185, Roma, Italy
[h]Università degli studi di Milano-Bicocca, Dipartimento di Fisica, Piazza delle Scienze 3, 20126 Milano, Italy
[i]Dipartimento di Fisica, Università degli Studi di Milano, Via Celoria, 16, Milano, Italy
[j]INFN–Sezione di Milano, Via Celoria 16, Milano, Italy
[k]Dipartimento di Fisica - Università di Genova, Via Dodecaneso, 33, 16146 Genova GE, Italy
[l]INFN–Sezione di Genova, Via Dodecaneso, 33, 16146 Genova GE, Italy
[m]IFAC–CNR, Via Madonna del Piano, 10, 50019 Sesto Fiorentino, FI, Italy
[n]Physics Department Pisa University, Largo B. Pontecorvo 3, 56127 Pisa (Italy)
[o]Department of Physics, California Institute of Technology, Pasadena, California 91125, U.S.A.
[p]Department of Physics and Astronomy, University of Pennsylvania, 209 south 33rd street, 19103, Philadelphia, Pennsylvania, U.S.A.
[q]INAF–OAS Bologna, Istituto Nazionale di Astrofisica - Osservatorio di Astrofisica e Scienza dello Spazio di Bologna, Via P. Gobetti 101, 40129, Bologna, Italy
[r]Dipartimento di Fisica, Università di Roma Tor Vergata, Via della Ricerca Scientifica, 1, 00133 Roma, Italy
[s]INFN–Sezione di Roma2, Via della Ricerca Scientifica, 1, 00133 Roma, Italy
[t]Instituto de Astrofísica de Canarias, C/Vía Láctea s/n, La Laguna, Tenerife, Spain
[u]Jet Propulsion Laboratory, California Institute of Technology, 4800 Oak Grove Drive, Pasadena, California, U.S.A.
[v]Departamento de AstrofÃŋsica, Universidad de La Laguna (ULL), E-38206 La Laguna, Tenerife, Spain
[w]INFN–Sezione di Milano Bicocca, Piazza delle Scienze 3, 20126 Milano, Italy
[x]Sub-department of Astrophysics, University of Oxford, Denys Wilkinson Building, Keble Road, Oxford OX1 3RH, UK
[y]INAF–Osservatorio Astronomico di Trieste, Via G.B. Tiepolo 11, Trieste, Italy
[z]Dipartimento di Fisica e Astronomia G. Galilei, Università degli Studi di Padova, via Marzolo 8, 35131 Padova, Italy
[A]Jodrell Bank Centre for Astrophysics, School of Physics and Astronomy, University of Manchester, Manchester, UK
[B]Universidad de Chile (UdC), Santiago, Chile
[C]Dipartimento di Fisica e Scienze della Terra, Università di Ferrara, Via Saragat 1, 44122 Ferrara, Italy
[D]INFN–Sezione di Ferrara, Via Saragat 1, 44122 Ferrara, Italy
[E]Cineca, Via Magnanelli, 6/3, 40033 Casalecchio di Reno BO, Italy
[F]Agenzia Spaziale Italiana, Via del Politecnico snc, 00133, Roma, Italy
[G]Argonne National Labs, 9700 S. Cass Ave, Lemont, IL 60439, USA
[H]INFN, Sezione di Bologna, Viale Berti Pichat 6/2, 40127 Bologna, Italy

E-mail: francesco.piacentini@roma1.infn.it

Abstract. The measurement of the polarization of the Cosmic Microwave Background (CMB) radiation is one of the current frontiers in cosmology. In particular, the detection of the primordial divergence-free component of the polarization field, the B-mode component, could reveal the presence of gravitational waves in the early Universe. The detection of such component is at the moment the most promising technique to probe the inflationary theory describing the very early evolution of the Universe. We present the updated performance forecast of the Large Scale Polarization Explorer (LSPE), a program dedicated to the measurement of the CMB polarization. LSPE is composed of two instruments: LSPE-Strip, a radiometer-based telescope on the ground in Tenerife, and LSPE-SWIPE (Short-Wavelength Instrument for the Polarization Explorer) a bolometer-based instrument designed to fly on a winter arctic stratospheric long-duration balloon. The program is among the few dedicated to observation of the Northern Hemisphere, while most of the international effort is focused into ground-based observation in the Southern Hemisphere. Measurements are currently scheduled in Winter 2021/22 for LSPE-SWIPE, with a flight duration up to 15 days, and in Summer 2021 with two years observations for LSPE-Strip. We describe the main features of the two instruments, identifying the most critical aspects of the design, in terms of impact into performance forecast. We estimate the expected sensitivity of each instrument and propagate their combined observing power to the sensitivity to cosmological parameters, including the effect of scanning strategy, component separation, residual foregrounds and partial sky coverage. We also set requirements on the control of the most critical systematic effects and describe techniques to mitigate their impact. LSPE can reach a sensitivity in tensor-to-scalar ratio of $\sigma_r < 0.01$, and improve constrains on other cosmological parameters.

Keywords: CMBR experiments; CMBR polarization; cosmological parameters from CMBR.

ArXiv ePrint: ...

Contents

1 Introduction

The Large Scale Polarization Explorer (LSPE) is designed to measure the polarization of the Cosmic Microwave Background (CMB) at large angular scales, and in particular to constrain the curl component of CMB polarization (B-modes). This is produced by tensor perturbations generated during cosmic inflation in the very early Universe [1, 2]. The level of this signal is unknown: current inflation models are unable to provide a firm reference value. However, the detection of this signal would be of utmost importance, providing a way to measure the energy-scale of inflation and a window on the physics at extremely high energies. While the level of CMB temperature anisotropy is of the order of 100 μK r.m.s. and the level of the gradient component of CMB polarization (E-modes generated by scalar - density perturbations) is of the order of 3 μK, the current upper limits for the level of B-modes polarization are a fraction of μK, corresponding to a ratio between the amplitude of tensor perturbations and the amplitude of scalar perturbations $r < 0.07$ (68% CL) [3]. The main scientific target of LSPE is to improve this limit. This, with the additional scientific targets of the mission are reported in the following list:

- a detection of B-modes of CMB polarization at a level corresponding to a tensor to scalar ratio $r = 0.03$ with 99.7% confidence level (CL);
- an upper limit to tensor to scalar ratio $r = 0.01$ at 68% CL;
- an improved measurement of the optical depth to the cosmic microwave background τ, measured from the large scale E-mode CMB polarization;
- investigation of the so called *low-ℓ anomaly*, a series of anomalies observed in the large angular scales of the CMB polarization, including lack of power, asymmetries and alignment of multipole moments;
- wide maps of foreground polarization produced in our galaxy by synchrotron emission and interstellar dust emission, which will be important to map the magnetic field in our Galaxy and to study the properties of the ionized gas and of the diffuse interstellar dust in the Milky Way;
- improved limits or detection of cosmic birefringence;
- study the quality of the atmosphere at Teide Observatory (Tenerife) for CMB polarization measurements.

Since the expected B-mode signal is smaller than the polarized foreground from our Galaxy, a wide frequency coverage is needed to monitor precisely the foregrounds at frequencies where they are most important, and to subtract them, in order to estimate the cosmological part of the detected B-mode signal. For the synchrotron foreground, prominent at frequencies below ~100 GHz, where atmospheric transmission and noise are favorable, a ground based instrument is the most effective strategy, while for the CMB and the interstellar dust foreground, prominent at higher frequencies, a stratospheric balloon mission is preferred, to cope with the poor atmospheric transmission and noise. For this reason, the LSPE program is based on the combination of two independent instruments: the Strip ground-based telescope, observing at 44 GHz, plus a 95 GHz channel for atmospheric measurements, to be implemented at the Teide Observatory (Tenerife); and the SWIPE balloon-borne mission, observing at 145, 220 and 240 GHz in a night Arctic stratospheric flight. The combined scanning strategies of the two instruments will produce full-frequency coverage over 37% of the sky, as shown in figure 1.

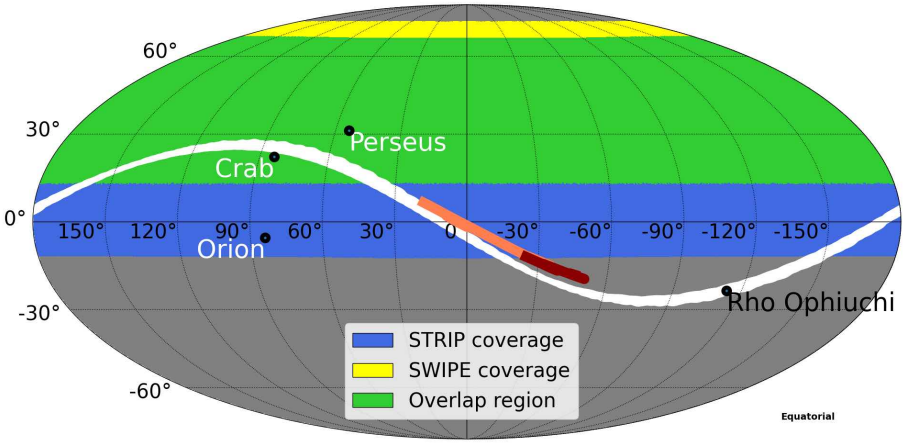

Figure 1. Map in Equatorial coordinates of the Strip-SWIPE coverage. In this map, the Strip zenith distance is set to 35°. The yellow area represents the SWIPE sky coverage, the blue area represents the Strip sky coverage, while the green area shows their overlap. The map also shows the position of the Crab and Orion nebulas, of the Perseus molecular cloud and the trajectories of Jupiter (orange), Saturn (dark red) and the Moon (white) from April 2021 to April 2023.

The overall design of the LSPE program is largely evolved since first proposal [4–6], and this paper presents its final design and expected performance. Section 2 describes the two instruments in some detail; section 3 shows the expected instrumental sensitivities; section 4 describes the major systematic effects, mitigation techniques and calibration; section 5 presents the methods used in the foreground cleaning and likelihood evaluation and reports the expected performances on cosmological parameters. Finally, section 6 draws conclusions.

2 The instruments

The LSPE program is based on the combination of two independent instruments: Strip and SWIPE. Table 1 reports basic parameters for the two instruments, in the baseline configuration. Map sensitivity is an approximated value, computed as the square root of $\sigma^2_{Q,U} = p\,\mathrm{NET}^2\,4\pi f_{\mathrm{sky}}/(T_{\mathrm{obs}}N_{\mathrm{det}})$, where $p = 1$ for Strip and $p = 2$ for SWIPE, to take into account that each detector is instantaneously sensitive to one polarization only, T_{obs} is the effective integration time, NET is the noise equivalent temperature of each detector, f_{sky} is the observed sky fraction, and N_{det} is the number of detectors. The power spectrum of the noise in polarization can be approximated by $\mathcal{N}_\ell^{E,B} = \sigma^2_{Q,U}/f_{\mathrm{sky}}$. More accurate performance is estimated using the instrument simulators, component separation, and cosmological parameters extraction algorithms, as described in sections 3 and 5. An update on the progress of the hardware development for the LSPE is provided in [7].

2.1 LSPE-Strip

LSPE-Strip is a coherent polarimeter array that will observe the microwave sky from the Teide Observatory in Tenerife in two frequency bands centred at 43 GHz (Q-band, 49 receivers) and 95 GHz (W-band, 6 receivers) through a dual-reflector crossed-Dragone telescope of ~ 1.5 m projected aperture.

The Strip array uses coherent technology exploiting low noise high electron mobility transistor (HEMT) amplifiers, together with high-performance wave-guide components. The instrument is cooled to 20 K by a two-stage Gifford-McMahon (GM) cooling system and integrated at the focal

Instrument	Strip		SWIPE		
Site	Tenerife		balloon		
Freq (GHz)	43	95	145	210	240
Bandwidth	17%	8%	30%	20%	10%
Angular resolution FWHM	20′	10′	85′		
Detector technology	HEMT		Multi-moded TES		
Number of polarimeters (Strip) / detectors (SWIPE)	49	6	162	82	82
Detector NET ($\mu K_{CMB}\ s^{1/2}$)	515	1139	12.6	15.6	31.4
Observation time	2 years		8 – 15 days		
Duty cycle	50%[1]		90%		
Sky coverage f_{sky}	37%		38%		
Map sensitivity $\sigma_{Q,U}$ (μK_{CMB} arcmin)	102	777	10	17	34
Noise power spectrum $(\mathcal{N}_\ell^{E,B})^{1/2}$ (μK_{CMB} arcmin)	171	1330	16	28	55

[1]We estimate as 50% the time dedicated to sky observations, including calibration sources. We split the remaining 50% as follows: (i) 15% of lost time due to bad weather, (ii) 15% of unusable data when the Sun will have an angular distance from the nearest feed less than 10° [8], 20% of time dedicated to relative calibration (see section 4.2).

Table 1. LSPE baseline instrumental parameters. Details are reported in tables 4 and 6.

plane of a continuously rotating 1.5 m aperture telescope. The polarimeters design allows to directly measure the Stokes Q and U parameters through a double-modulation scheme. This design ensures excellent rejection of $1/f$ noise from amplifier gain fluctuations as well as of temperature-to-polarization leakage, without the need to introduce extra optical elements to modulate the polarized signal.

The main objective of Strip is to accurately measure Galactic synchrotron emission in the LSPE sky region in Q-band. Recent studies [9] show that the polarized synchrotron emission is significantly structured and characterized by non-trivial variations in its spectral index. Deep measurements at 43 GHz, complemented by lower frequency data, are crucial to constrain synchrotron contamination in the foreground minimum accounting for spectral index variations. Furthermore, achieving a resolution of $\sim$ 20 arcmin will provide key information on the spatial properties of synchrotron foreground.

The W-band array, composed of 6 modules, will complement the Q-band data in monitoring the atmospheric load and fluctuations (mostly due to water vapor) during the Strip observations. Atmospheric effects in Q-band can be effectively monitored by measurements in W-band, where the water vapor component is significantly higher. Note anyway that at the Teide Observatory the atmospheric contamination of Q-band data is clearly dominated by O_2, which is stable spatially and with time. Yet the W-band channels will help to mitigate Q-band atmospheric fluctuations, expected to be of the order of $\sim$ 2 K.

2.1.1 Observation Site

Strip will be deployed at the Teide Observatory in Tenerife, at an altitude of 2400 m above sea level. The site provides excellent observing conditions and has been well-tested for astronomical observations for more than 30 years. The median precipitable water vapour is 3.5 mm, reaching values below 2 mm during 30% of the time [10]. The inversion layer lies below the observatory for approximately 80% of the time.

The observatory has a long tradition in CMB research, including past experiments like the Tenerife radiometers [11], the IAC-Bartol [12], the JBO-IAC two-element interferometer [13], the COSMOSOMAS experiment [14] and the Very Small Array interferometer (VSA [15]). The Strip telescope will be installed inside an aluminium ground screen to limit interference and ground-spill. The basement full structure will be protected by a sliding roof that will cover the whole enclosure.

In addition to serving as low frequency monitor for LSPE, Strip also will complement two existing CMB experiments in Tenerife, QUIJOTE [16] and GroundBIRD [17], by observing in different frequency bands: 10–40 GHz for QUIJOTE, 40–95 GHz for Strip, and 145–225 GHz for GroundBIRD. All three Tenerife projects (QUIJOTE, LSPE-Strip and GroundBIRD) aim at measuring approximately the same area in the Northern sky and at degree scales, opening the possibility of future combined analyses, including useful redundancy for cross-checks of systematic effects. Strip measurements are currently scheduled to start during Summer 2021 and last two years.

2.1.2 Observation strategy

The Strip telescope will scan the sky at a constant zenith angle, nominally 20°, with 1 r.p.m. spin rate. This strategy will allow us to minimize atmospheric effects and to cover about 38% of the Northern sky, thus ensuring a large overlap with the SWIPE observations. After two years operations with 50% duty cycle we will reach a sensitivity of $\sim$102 μK_{CMB} arcmin at 43 GHz and $\sim$777 μK_{CMB} arcmin at 95 GHz. Our duty cycle does not account for down time due to the Moon, glitches, Radio-Frequency Interference (RFI), or other unpredictable instrument-specific anomalies, thus moving our estimate somewhat on the optimistic side. A breakdown of our estimated data loss is given in the footnote of table 1.

2.1.3 Telescope and mount structure

The Strip telescope consists of two reflectors, a parabolic primary mirror and hyperbolic secondary mirror, arranged in a Dragonian cross-fed design, originally developed for the CLOVER experiment [18]. This configuration preserves polarization purity on the optical axis and gives low aberrations across a wide, flat focal plane. The projected diameter of the main reflector is 1.5 m and the entire system has an equivalent focal length of 2700 mm, resulting in $\sim$ f/1.8.

The telescope is surrounded by a co-moving baffle made of aluminum plates coated by a millimetre-wave absorber, which reduces the contamination due to straylight. The optical assembly is installed on top of an alt-azimuth mount, which allows the rotation of the telescope around two perpendicular axes to change the azimuth and elevation angle. An integrated rotary joint will transmit power and data to the telescope and the instrument, and will allow a continuous spin as required by the scanning strategy. A general view of the Strip system is shown in figure 2.

The telescope provides an angular resolution of $\sim 20'$ in the Q-band and $\sim 10'$ in the W-band. The feedhorn array is placed in the focal region, ensuring no obstruction of the field of view. All the modules are optimally oriented according to the shape of the focal surface, with illumination centred on the primary mirror. The two mirrors determine the main beam shapes of the Strip detectors, while the shielding structures affect the near and far sidelobes [19].

Optical performance. The optical assembly has been modelled with the GRASP[1] software and the model includes the nominal reflectors, the focal plane unit, the IR filters, and the shielding structures. The model is also able to reproduce the dual circular polarization antenna-feed system [20].

[1] https://www.ticra.com/software/grasp/

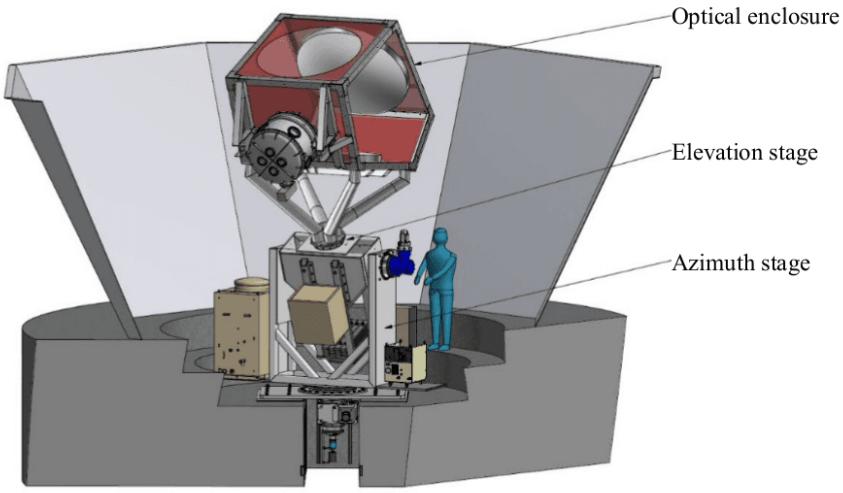

Figure 2. LSPE-Strip optical system overview. The three-axis mount allows the rotation of the optical assembly around the boresight direction. The mirrors are held inside a co-moving baffle (translucent red).

	43 GHz	95 GHz
Angular resolution	21′	9.5′
Directivity	54.7 dBi	61.4 dBi
XPD	40.8 – 44.5 dB	44.1 – 46.6 dB
Ellipticity.....	1.003 – 1.033	1.006 – 1.041
Field-of-view	±5°	

Table 2. Main beam parameters for the two Strip channels.

Main beam radiation patterns have been simulated using the Physical Optics (PO) method, which is needed to correctly model the detector patterns in the far field. Given the off-axis configuration, the main beams are characterized by several parameters, as the angular resolution, the ellipticity, the main beam directivity, and the cross-polar discrimination factor (XPD). The main parameters that characterize the telescope response are reported in table 2.

Side-lobes have been computed using the Multi-Reflector Geometrical Theory of Diffraction (MrGTD). While less accurate than PO, this ray-tracing technique is much more efficient and it is able to predict the full-sky radiation pattern of complex optical systems. The 4π radiation patterns show unevenly distributed features that are due to multiple reflections inside the shielding structure and rays entering the feedhorns without any interaction with the reflectors. Each contribution has been analyzed separately and then combined in an integrated model beam. We find that the near and far sidelobe level is always better than −55 dB at 43 GHz and better than −65 dB at 95 GHz.

2.1.4 Instrument and cryogenics

The Strip focal plane array of corrugated feed horns is placed inside the dewar surrounded by a radiative shield cooled to 80 K by the cooler first stage (see the left-hand panel of figure 3). Copper thermal straps connect the focal plane and the cooler cold head allowing the polarimeter chain to be cooled down to 20 K. The cryostat aperture is an ultra-high molecular weight polyethylene (UHMWPE)

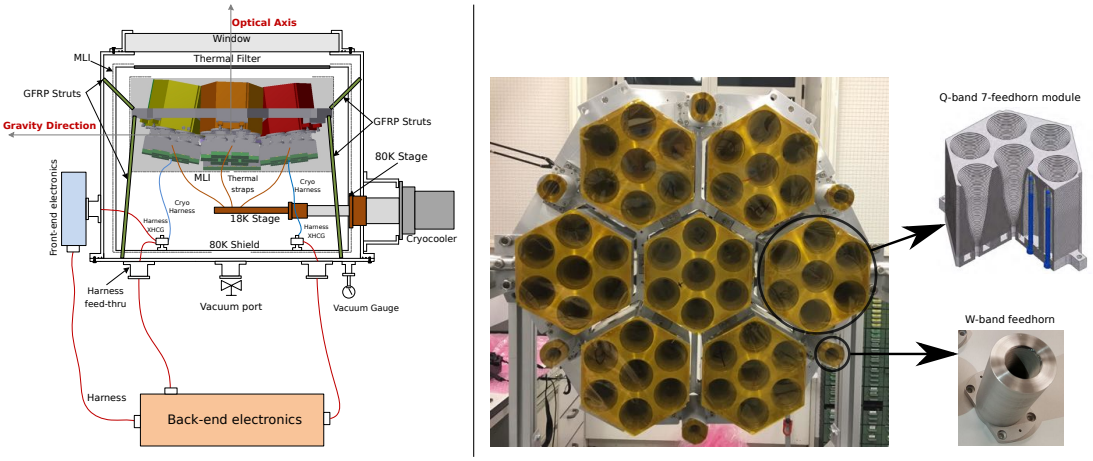

Figure 3. *Left*: schematics of the Strip instrument. The focal plane array is inside the cryostat surrounded by the 80 K shield and thermally connected to the cooler cold head. *Right*: the complete Strip focal plane array with 49 feedhorns in Q band and 6 heedhorns in W band.. We also show a cutaway of one Q-band module (*top*) and the detailed view of one of the six W-band feedhorns.

window followed by 13 IR filters at 150 K (one filter for each horn at 95 GHz and one filter for each 7-horns module at 43 GHz) to reduce the radiative load from the 300 K environment.

The detector assembly is based on coherent polarimeters connected to an optical chain constituted of corrugated feedhorns, each coupled to a polarizer-orthomode transducer (OMT) system at 43 GHz and to a septum polarizer at 95 GHz [21].

Feedhorns. The feedhorns are designed implementing a dual profile to obtain an optimal illumination of the secondary with a limited feed size, and are manufactured in aluminum using the platelet technique [22]. The right panel of figure 3 shows a picture of the entire Strip focal plane, with the 49 Q-band feedhorns arranged in 7-unit modules surrounded by the six W-band feedhorns. A cutaway of one of the Q-band modules and a detailed view of one of the W-band feedhorns are also presented. In the cutaway it is possible to appreciate the platelet structure of the module and the tightening screws that allowed to assemble the horns without the need of bonding material or thermal brazing.

Polarizers and OMTs. Each feedhorn is connected to a polarizer system that converts the two orthogonal components of the electric field, (E_x, E_y) into right- and left-circular polarization components, $\left[(E_x + i\,E_y)/\sqrt{2}, (E_x - i\,E_y)/\sqrt{2}\right]$, which propagate through the polarimeter module. This conversion is obtained differently in Q and W-bands.

In Q-band we convert linear to circular polarization using a groove polarizer [23] connected to a platelet OMT [24]. In figure 4 we show the complete set of Q-band polarizers (left panel) and OMTs (right panel) implemented in the Strip focal plane. This solution allowed us to obtain a very good measured performance in terms of transmission ($\gtrsim -0.5$ dB), reflection (< -25 dB), cross-talk (~ -40 dB) and leakage from intensity to polarization (~ -30 dB).

Each W-band channel incorporates a septum polarizers characterized by a reflection of < -20 dB and a leakage of intensity to polarization of the order of ~ -13 dB. The detailed design and performance of these components, originally used by the QUIET 95 GHz instrument [25], can be found in [26].

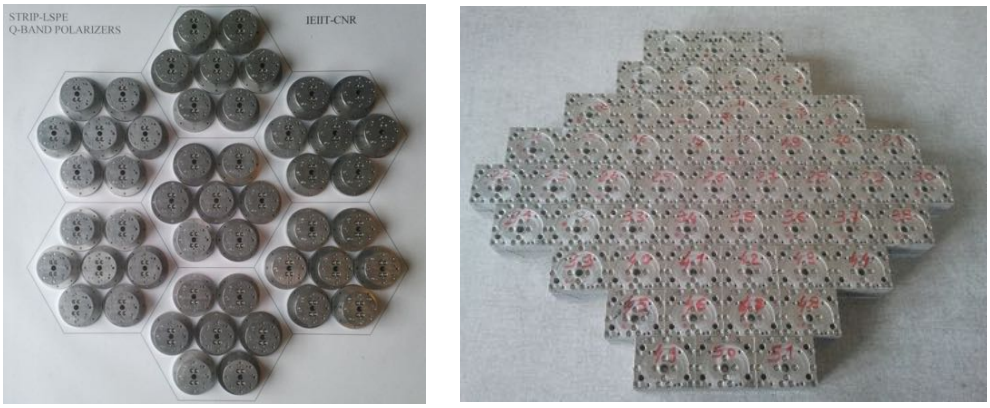

Figure 4. *Left:* the 49 Strip Q-band polarizers arranged according the 7-module feedhorn footprint. *Right:* the 49 Strip Q-band platelet OMTs

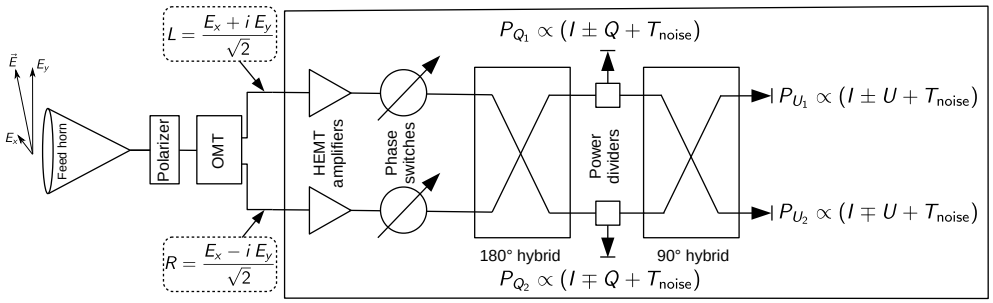

Figure 5. Schematics of the Strip polarimeters operation principle. The figure also shows the main mathematical relationships among the detected power at the four diodes, $P_{Q_{1,2}}, P_{U_{1,2}}$, the Stokes parameters defined in the polarizer reference frame, I, Q, U and the polarimeter noise temperature, $T_{\rm noise}$.

Polarimeters. The Strip Q-band channel uses a combination of the original 19 QUIET Q-band modules [27] and additional 30 units that were developed according to the same design. The W-band channel uses 6 QUIET polarimeters selected among those with the best performance. The diagram in figure 5 shows the operation principle. If two circularly polarized signals propagate through a symmetric 180° hybrid, the power detected at its output is a combination of I and Q Stokes parameters, with Q having opposite signs at the two detectors. The detected power at the output of a second, 90° hybrid coupler yields a combination of I and U, with U appearing with opposite signs. The design takes full advantage of the coherent nature of the signal, implementing a double modulation scheme to minimize residual systematic effects. This strategy allows to recover both Q and U from a single measurement, after combining the two linearly polarized components of the input field, E_x and E_y, into left and right circular polarization components.

Ahead of the first hybrid, two multi-stage Indium Phosphide (InP) HEMT amplifiers provide about 50 dB amplification while two phase switches shift the signal phase between 0° and 180° and allow to demodulate the measurements.

There are two different kinds of demodulation. A fast ($\sim$ 4 kHz) demodulation, provided by one of the two phase switches that flips the signs of Q and U at each of the four diodes (see figure 5), allows to remove effectively the effect of amplifier gain fluctuations. A slow (50 Hz) demodulation,

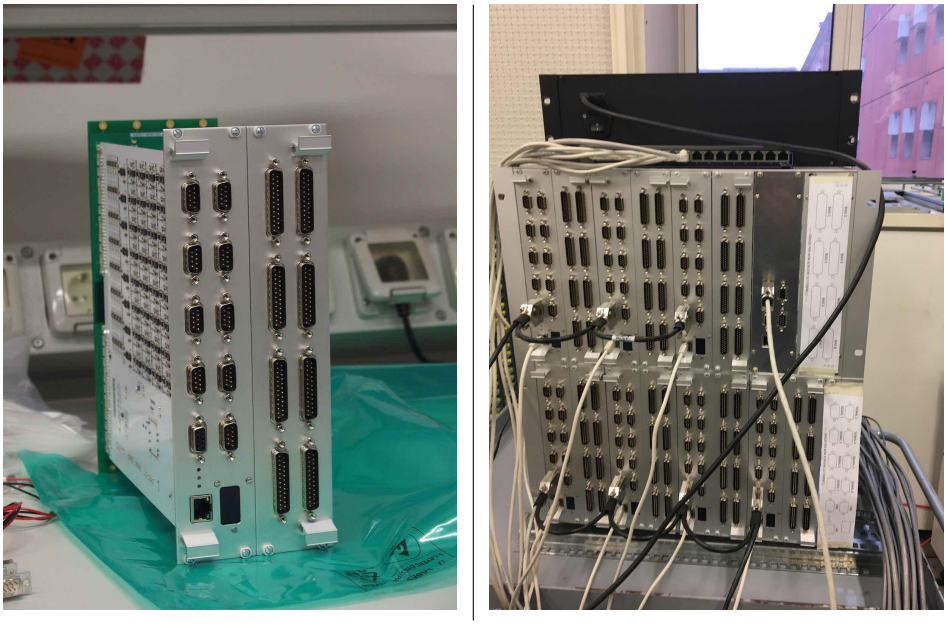

Figure 6. *Left*: one of the 7 modules of Strip electronics composed by one bias board on the right and one data acquisition and logic board (DAQ). Both are connected to a back-plane (in green) for stabilized power supply and data exchange between the two boards. *Right*: the two 6U 19 inches racks containing the Strip electronics during the final tests.

provided by the second switch that flips the sign between detector pairs, removes any $I \rightarrow Q, U$ leakage arising from asymmetries in the phase switches attenuation.

The correlation units are packaged into square brass modules about 1 cm thick and with a footprint of $\sim 5 \times 5\,\mathrm{cm}^2$ in Q-band and $\sim 2.5 \times 2.5\,\mathrm{cm}^2$ in W-band. Each complete polarimetric chain from the feed to the detectors will be cooled down to 20 K by the Strip cryogenic system.

Electronics. The Strip electronics provides the full biasing and acquisition of the 55 polarimeters on the focal plane. It consists 7 pairs of boards that drive and acquire data from 8 polarimeters each. Each pair contains one bias board and one Data AcQuisition and logic board (DAQ), shown in the left panel of figure 6.

The bias voltages are set and monitored by the bias board that controls the HEMT low noise amplifiers (LNAs) and phase switches. All the phase switches of all the 7 board pairs are synchronized by a master-clock signal generated and distributed by the GPS and Master-Clock board through a dedicated daisy-chain cable. The bias board can operate the LNAs in open- or closed-loop. In open loop the drain and gate voltages of every transistor are set according to an optimum configuration found during the unit- and system-level tests, and the drain current is simply monitored through the bias house-keeping. In this case bias voltages are susceptible to variations of the focal plane temperature. In closed loop we set the drain voltages and currents, and a completely analogue loop adjusts the gate voltages to keep the desired currents. The closed loop mode is useful in case of excessive temperature instability and its use will be particularly important during the commissioning phase.

The DAQ boards have two functions: they interact with the main computer via telemetry-telecommands and acquire the data generated by the four detectors of each polarimeter. Each board controls 8 polarimeters and receives and stores their bias settings from the main computer via Ether-

net network. In this way, the operations can autonomously restart in case of communication loss after a black-out. The bias settings are then passed to the bias board. Each DAQ board acquires data from 32 detectors at a rate of 1 MHz, demodulates the scientific data at rate of the fast phase switch rate (4 kHz), prepares the data packets with scientific signals, housekeeping data and time tags obtained from the GPS/master clock and sends the data via Ethernet to the main computer for storage.

A field programmable gate array (FPGA) carries out the mathematical operations as well as the digital-to-analog (DAC) and analog-to-digital (ADC) conversions, while a microcontroller handles the communication with the main computer, decodes and routes the commands towards the FPGA and assembles the data packets. The data stream produced by the seven DAQ boards is $\sim$ 2 Mb/s, well below the maximum Ethernet capability.

The full electronics occupies two 6U 19 inches racks (right panel of figure 6) that will be positioned close to the dewar and protected by two IP55 grade cabinets.

2.2 LSPE-SWIPE

LSPE-SWIPE (Short-Wavelength Instrument for the Polarization Explorer) is a mm-wave polarimeter operated onboard a stratospheric balloon. The general idea of SWIPE is to use a cryogenic rotating Half-Wave Plate (HWP) to modulate the incoming polarized radiation and to maximize the sensitivity to CMB polarization at large scales using a very wide focal plane populated with multi-moded bolometers. The spectral coverage of SWIPE has been optimized to be very sensitive to CMB polarization with one broad-band channel matching the peak of CMB brightness (145 GHz, 30% band), and to be able to monitor and separate the signals from interstellar dust (the main polarized foreground at this frequency) by monitoring it with two ancillary, narrower channels at 210 and 240 GHz. These are dedicated to measure the slope of the specific brightness of interstellar dust. The focal planes of SWIPE are large enough that a total of 8800 modes of the incoming radiation are collected by the multi-moded 326 detectors, thus boosting the sensitivity of the polarimeter to unprecedented levels for such a comparatively low number of detectors. The detectors arrays are cooled to 0.3 K by a large wet cryostat, which also cools the polarization modulator and the entire telescope. The cryostat is mounted in a frame, the gondola, providing accommodation for an attitude control system, the power system and electronics. The gondola interfaces to the flight train of the stratospheric balloon through an azimuth pivot allowing for azimuth spin and/or scan. A general view of the SWIPE instrument is shown in figure 7. LSPE-SWIPE measurements are currently scheduled for Winter 2021/22.

2.2.1 Winter polar balloon flight

LSPE-SWIPE is designed to fly on a stratospheric long-duration balloon in the arctic winter. Stratospheric balloon altitudes (about 35 km above sea level) are needed to avoid most of the atmospheric emission, which is relevant at 145 GHz and very important at higher frequencies. A winter launch guarantees the possibility to exploit the absence of the Sun and cover a large fraction of the sky by spinning the full payload, allowing to explore efficiently the CMB polarization anisotropy at large angular scales. It also ensures higher stability of the observing conditions, due both to the thermal stability of the instrument and to the lowest residual turbulence in the atmosphere.

The instrument is designed for a 15 days long flight. This long duration is needed to reach the sensitivity which matches the scientific goal of the LSPE experiment. Options for launching in the polar night are at the moment only possible from the Northern Hemisphere, due to the logistics difficulties related to the access to Antarctic regions during austral winter. In particular, two possible launching stations are Longyearbyen, in Svalbard islands (Norway), with a latitude above 78.2°N, and Kiruna (Sweden) at a latitude of 67.8°N. Several launches have been performed from Longyearbyen, with different balloon and payload sizes, both in Summer and in Winter over the last few years.

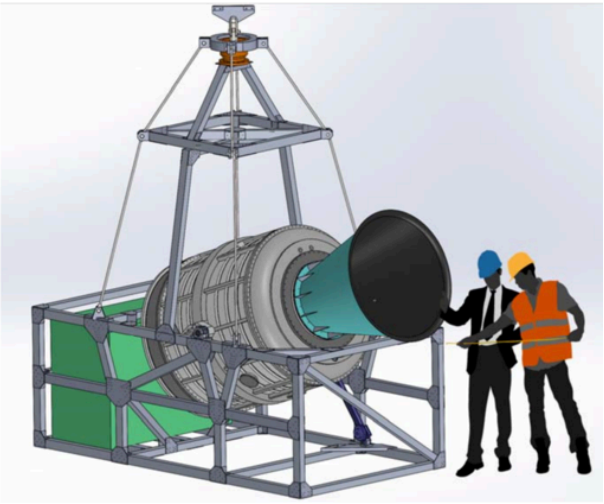

Figure 7. LSPE-SWIPE overview. The instrument is contained in a large liquid Helium cryostat, which also contains the optical elements, including the HWP based Stokes polarimeter. The on-board electronics and the Lithium batteries based power system are contained in an Aerogel insulated box, to optimize thermal balance.

Kiruna offers an established alternative, although at lower latitudes. Stratospheric balloon flights are organized by the Swedish Space Corporation in the Esrange Space Center.

Such a long duration flight in the winter, while being appealing from the scientific point of view, is very demanding in terms of power system and thermal balance. A series of technological test flights has been carried out over the years, as reported in [28–33]. All the LSPE-SWIPE parts are designed to cope with temperatures as low as −90 °C, except the battery packs and part of the electronics, which are contained in a thermally insulated box.

2.2.2 Power Supply

For a long-duration night-time flight, a relatively cheap, consolidated, high energy-density power-supply solution is based on lithium batteries. The total power budget of the SWIPE instrument is $\sim$ 370 W, and the energy necessary for the entire mission is $\sim$ 0.48 GJ. This is stored in a stack of $\sim$ 3500 cells (each 14 Ah @ 3.3 V). Due to the low internal resistance of these cells, and the fact that their capacity decreases at low temperatures, it is necessary to keep the cells warm (at a temperature $>$ 0 °C) during the flight. This is obtained bt hosting the batteries in the same box hosting the electronics of the experiment, and in good thermal contact. The box is insulated from the cold external environment by a blanket made of three layers of metal reflective foil separated by two thick ($\sim$ 2.5 cm) layers of aerogel. According to the thermal model, with 200 W of power dissipated in the electronics inside the box, and an external temperature of 200 K, the internal temperature is maintained at 280 K. A prototype of this power and thermal insulation system was flown in a winter arctic balloon in December 2017 [33], and further tests are planned for the future.

2.2.3 Gondola and pointing system

The gondola is a simple riveted frame of aluminum beams, hosting all the components of the payload and of the flight system, and structurally optimized to withstand an acceleration of 10 g (g = gravitational acceleration) at the opening of the parachute after the flight termination. The telescope attitude is controlled by the attitude control system (ACS). Its main purpose is to spin in azimuth the entire gondola. The azimuth pivot separates the payload from the flight chain, and is based on thrust

bearings and a torque motor. The motor torques directly against the flight chain, to obtain an azimuth spin rate up to 10 °/s. Mechanically and electrically, the system is very similar to the ones used in ARGO [34], BOOMERanG [35, 36], Archeops [37], OLIMPO [38–40], and described in detail in [41–43]. Given the measured friction of the thrust ball bearing, we expect to use up to ∼ 70 W to rotate the ∼ 2000 kg payload at the 10 °/s scan speed. The azimuth speed is sensed by a laser-gyroscope, the signal of which is compared to the desired spin rate, in a feedback loop controlling the current in the torque motor. The elevation of the boresight can be changed by tilting the entire cryostat, using a geared DC motor driving a linear actuator with linear recirculating ball bearing. The pointing reconstruction is based on a high altitude GPS receiver to obtain geographical coordinates and on two orthogonal fast star sensors [44], the same successfully used for the Archeops flight [45], for the celestial coordinates of the boresight. The system allows for pointing reconstruction with ∼ arcmin accuracy.

2.2.4 Cryostat

SWIPE makes use of a custom-designed main cryostat with a bath of 250 liters of superfluid helium, connected to the external low-pressure environment to operate at 1.6 K. The cryostat shell, the internal shields and the LHe tank are all made of aluminum alloys, to reduce their mass, as developed for the cryostats used in the ARGO [46], BOOMERanG [47], PILOT [48] and OLIMPO [49] balloon-borne instruments. Two vapor-cooled intermediate shields, separated by super-insulation blankets, are used to minimize the radiative heat load on the LHe bath. The main cryostat provides the base temperature to cool down the polarization modulator and the optical system, and to operate a ^{3}He evaporator [50]. The latter cools down to 0.3 K the two focal plane arrays, as required to operate the SWIPE bolometric detectors. The hold time forecast for the LHe in the main cryostat is ∼ 20 days, while the ^{3}He refrigerator has a hold time of ∼ 7 days, and can be recycled in flight. In order to minimize the radiative load on the detectors, the 600 mm diameter window has been designed in a similar way as the one used by the EBEX group [51], and, less recently, in [52] and in [53]. In practice, a thick UHMWPE [54] window used for laboratory tests is removed at float, leaving only a very thin ($\ll \lambda$) Mylar window to withstand the small pressure difference between the cryostat vacuum and the stratospheric pressure. The thick window also implements a highly reflective filter to operate the receiver on the ground under radiative loadings representative of the stratospheric environment. Just before the termination of the flight, the motor unit is remotely operated again to put the thick window back in place for a relatively safe receiver landing.

2.2.5 Optical system

The optical system of LSPE-SWIPE (figure 8) consists in a single-lens, 490 mm aperture refractor telescope, focusing incoming radiation on two large curved focal planes, split by a large wire grid (WG) polarizer. Each focal plane is populated with 163 multi-moded feedhorns, each feeding a spider-web Transition Edge Sensor (TES) bolometer. Polarization modulation is obtained by a cryogenic 500 mm wide rotating half-wave-plate (HWP) which is placed before the lens and after window and filters in the optical system.

The configuration fulfills our requirements with a low cross-polarization ($< 1\%$) and a controlled instrumental polarization (including an absorption component $< 0.04\%$ and an extremely low, and stable, emitted component by the use of a cold telescope). These goals are reached at the edge of the corrected focal plane for all the 3 bands and they are totally negligible on axis. Besides the 490 mm diameter lens the optics is completed by a 460 mm diameter cold stop close to the lens (corresponding to an entrance pupil of 487 mm diameter). The FOV, 20° wide, is split by a 500 mm

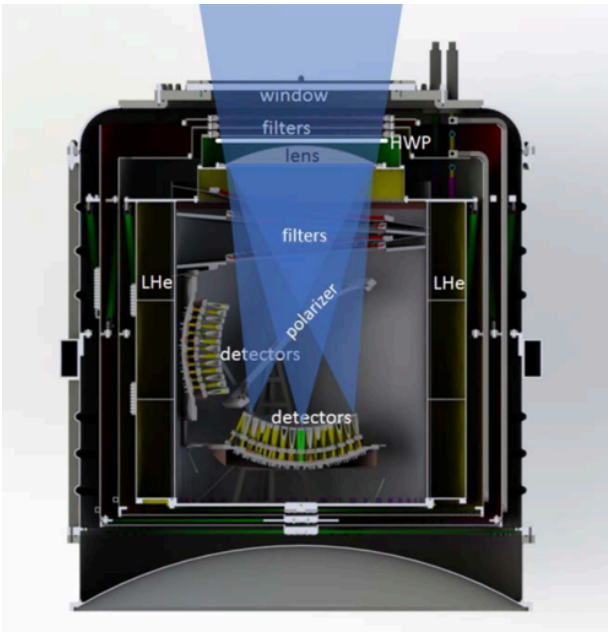

Figure 8. LSPE-SWIPE cryostat and optical system. Radiation enters from the top window, passes across filters, Half-Wave Plate, lens, and other filters. It then is split by the large wire grid and collected in the two curved focal planes.

diameter 45° tilted wire grid in 2 curved focal planes (CFP_T and _R) 300 mm in diameter both with a f-number equal to f/1.75. The full optical system is kept at cryogenic temperature in the LSPE-SWIPE cryostat, in order to minimize its radiative loading on the detectors and to mitigate the signals due to the rotation of the emissive HWP.

The radiation is coupled to the detectors by means of smooth conical horns feeding multi-moded waveguides [55]. The waveguides select a frequency-dependent number of modes, thus determining the effective pixel throughput. Under the assumption that radiation detection is based on purely incoherent processes on the detector absorber, the phase relation among the coupled modes is not relevant to determine the coupling efficiency. Therefore, electromagnetic modelling of the horn-waveguide assembly can be easily performed by solving one reverse-propagation problem per each of the coupled modes selected by the waveguide. A far-field calculation of the field solution at the horn aperture then yields the individual contribution of each mode to the horn response, and the full multi-moded response is then computed as a power summation over the coupled modes. This operation has been performed through the Ansys HFSS[2] software, and the calculated beam profile for the SWIPE horns is shown in figure 9. Here the contributions from the individual modes have been evenly weighted, as expected under energy equipartition conditions, and confirmed by numerical simulation of the absorber/cavity sub-system (see section 2.2.7). A measurement of the feed angular response is reported in [56].

Integration of the numerically evaluated profile times the horn effective area yields a value very close to $A_{\rm eff}\Omega_{\rm tot} = N_{\rm modes}(r_{\rm wg}, \nu)\lambda^2$, where $N_{\rm modes}(r_{\rm wg}, \nu)$ is the number of propagating wave solutions (i.e. modes with imaginary wavenumber) in a cylindrical waveguide of radius $r_{\rm wg}$ at frequency ν, and λ is the free-space wavelength of monochromatic radiation. This result is expected under equipartition conditions, where each coupled mode provides a λ^2 contribution to the system throughput. In

[2] https://www.ansys.com

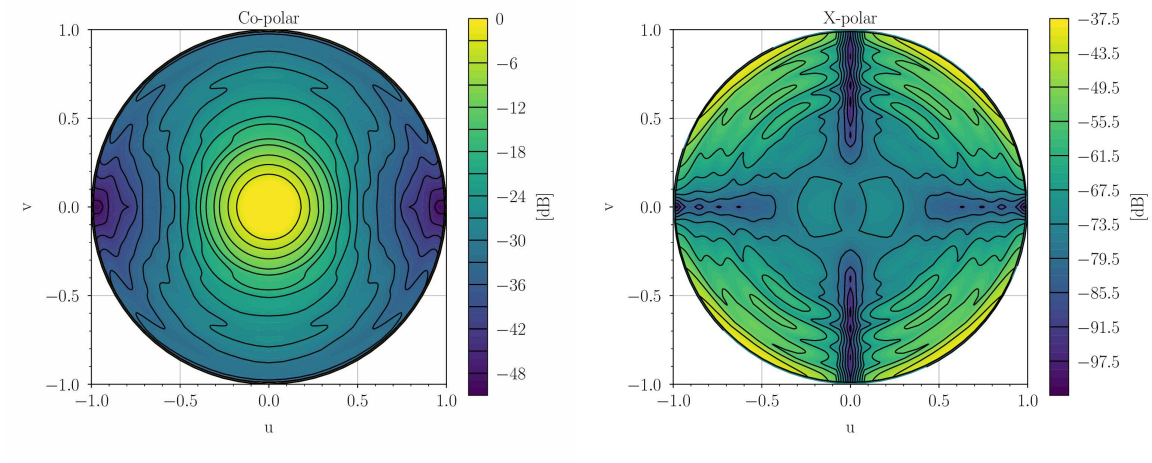

Figure 9. Simulated beam response of the SWIPE multi-moded horns. Radiation is propagated into the far field with linear polarization parallel to the v axis in the plane of the horn aperture, corresponding to the $\phi = 90°$ axis in the far field. Co-polar and cross-polar patterns have been calculated following Ludwig's third definition in [57] and are mapped against $u = \sin(\theta)\cos(\phi)$, $v = \sin(\theta)\sin(\phi)$. Contours are shown every 3 dB for the co-polar pattern and every 6 dB for the cross-polar pattern, which tops at −37.6 dB below the level of on-axis co-polar response.

addition, since we use a full-field polarizer to split polarization in two independent focal planes, the polarization properties of the individual pixel assembly are irrelevant for the end-to-end performance evaluation. Therefore, no concern arises due to the co-polar and cross-polar response behavior of the horns.

In order to simplify the design and production cycle of the horns, no additional optimization is performed at the pixel level. Instead, further suppression of power at large angles from the sky is obtained by heavily over-illuminating the cold aperture stop (with an edge taper of −10 dB at 145 GHz). The multi-moded beam of each horn thus ensures a very uniform illumination pattern of the telescope lens, maximizing the aperture efficiency of the telescope, while unwanted power pickup in the horn sidelobes is mitigated through implementation of cold, stable, highly absorptive surfaces inside the telescope tube. Additional large-angle pickup due to strong beam truncation at the aperture will be mitigated through an absorptive external baffle.

This multi-moded approach ensures an optimal tradeoff between the need for a conspicous number of independent focal plane elements and the net sensitivity of the individual pixels. This comes at the price of a lower angular resolution of the receiver, which is acceptable since the main observational target of SWIPE is polarization detection at large scales, from ∼2° to one third of the full sky.

2.2.6 Polarization modulator

In order to modulate the polarized component of the signal, LSPE-SWIPE adopts a Stokes polarimeter based on a Half-Wave Plate built of metal mesh metamaterials. This technology has been developed by the Astronomy Instrumentation Group at the Department of Physics and Astronomy of the Cardiff University [58]. The mesh HWP consists of anisotropic metal grids, stacked together and embedded into polypropylene, which mimic the behaviour of a birefringent plate [59, 60]. The geometry and the spacing of the grids are chosen in such a way to provide high in-band transmission (above 95%) and high polarization modulation efficiency (at 98% level) across all the bands.

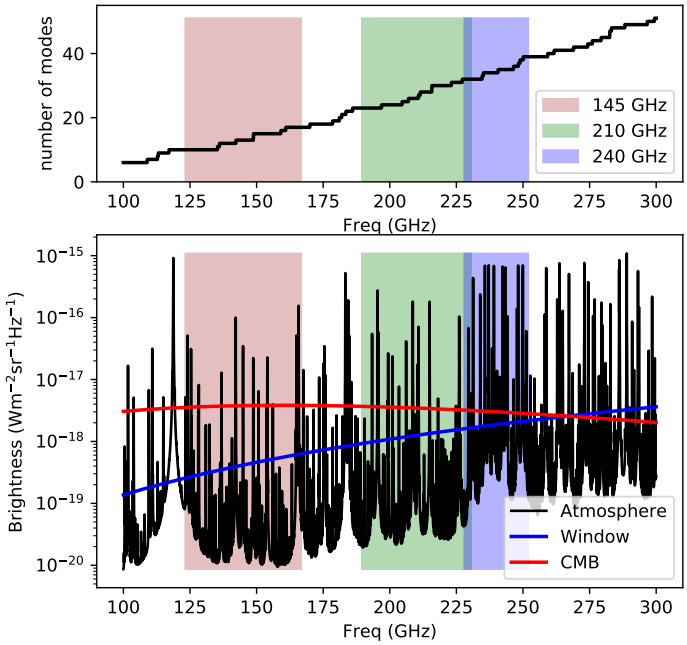

Figure 10. *Top*: LSPE-SWIPE number of modes coupled to the multi-moded optical assembly, as function of frequency. The three bands centered at 145, 210, 240 GHz are also shown. *Bottom*: LSPE-SWIPE bands and expected brightness from atmosphere, cryostat window and CMB.

Due to the requirements of cryogenic temperature and continuous rotation of the HWP, we selected a superconducting magnetic bearing (SMB) [61, 62] as the technology to spin the HWP and to modulate the polarized signal at a sufficiently high rate (∼ few Hz). An innovative frictionless clamp/release device [63], based on electromagnetic actuators, keeps the rotor in position at room temperature, and releases it below the superconductive transition temperature, when magnetic levitation works properly. A simple method to measure the temperature and levitation height of the HWP rotating at cryogenic temperatures was developed specifically for LSPE-SWIPE [64].

2.2.7 Detectors

LSPE-SWIPE adopts TES detectors. In order to take advantage of the multi-moded coupling, radiative power propagated from the feedhorns into the mode-filtering waveguides must be absorbed by the detector with as low impedance mismatch as possible for all the propagated modes. One way to fulfill this requirement is to compress the effective wavelengths of the coupled modes into a narrower bandwidth by progressively re-enlarging the waveguide cross-section into a larger terminated cavity (flared waveguide), where a 15 mm large spider-web absorber collects the power for detection by the TES. This solution has been validated through HFSS, providing a mode-dependent, frequency-dependent S_{11} scattering parameter[3] evaluation of the pixel assembly along the path from the waveguide to the absorber. The relative S_{11}-parameter dispersion for the 150 GHz band is about 2% over the coupled modes and frequencies, with an average return loss of −22.6 dB when the cavity termination is set

[3] Input port reflection coefficient.

to a quarter of the average free-space wavelength of the band collected by the detector, and the absorber impedance is $\sim 300\,\Omega$. This result, to be validated also through experimental verification of the pixel performance, is used here to support the hypothesis that the main impact of the broadband performance evaluation for SWIPE is the variable number of modes $N_{\rm modes}(r_{\rm wg}, \nu)$ coupled by the waveguide when fed with broadband radiation. Figure 10 illustrates the coupled modes as a function of frequency, and the selected bands; in the bottom panel, it shows the power hitting into the system entrance, with contribution from the CMB, the atmosphere and the cryostat window. These are the input to the noise calculation analysis reported in section 3.3 and in table 6.

The TES bolometer is a single Si chip $15 \times 15\,{\rm mm}^2$ with Au absorber deposited on a central free-standing Si_3N_4 membrane, 1 μm thick and 10 mm diameter. After the TES and Au absorber film have grown, the membrane is first etched in a shape of a 8 mm diameter circular spider-web supported by 32 narrow legs and then suspended by means of Deep Reactive Ion Etching of the silicon beneath. The TES is located aside the circular spider-web and is in strong electronic contact with the external perimeter of the gold absorber. The TES consists of 120 nm of a Au-Ti bilayer, which is manufactured taking care to maintain a process temperature profile below 100 °C, to ensure a superconducting to normal transition at $T_c = 500 - 550\,{\rm mK}$. In fact, it has been observed that high process temperatures reduce T_c towards its bulk value of $350 - 400\,{\rm mK}$, as demonstrated in [65]. These operating temperatures represent an optimal compromise between the SWIPE's bath temperature of 300 mK and the detector saturation limits due to the high optical power (order of 10 pW) of the multi-mode configuration. The thermal conductance G, in the range of $65 - 100\,{\rm pW\,K^{-1}}$, was measured in the first prototypes that have been operated at a base temperatures of about 350 mK. The effective time constants in Electro-Thermal Feedback (ETF) regime were evaluated from the frequency response functions at a sinus sweep excitation to be around $20 - 33$ ms, about a factor $2 - 3$ larger than the ones expected by the model. In these working points the thermal fluctuation noise equivalent power, NEP, is about $3 \times 10^{-17}\,{\rm W\,Hz^{-1/2}}$ (see section 3.3 for details).

The left panel of figure 11 shows the distribution of detectors in one of the two equivalent focal planes. The payload rotates so that the scanning direction is along the x axis in the figure. The right panel of figure 11 shows the LSPE-SWIPE large spiderweb TES bolometer integrated in the backshort of the microwave cavity.

2.2.8 Readout

The 326 TES bolometers are read-out by Superconducting Quantum Interference Devices (SQUIDs) using a Frequency-Domain Multiplexing scheme (FDM), with each DC-SQUID sensing 16 TES [66]. In the FDM scheme a group of detectors is readout with a single SQUID by connecting in parallel several RLC chains in which R is given by the TES variable resistance, and the LC filters define different frequencies. A single signal containing all the different frequencies is therefore needed to bias all TESs simultaneously. The detectors modulate the signal which is in turn sent to the SQUID input, amplified and demodulated by a digital electronics. A 16× multiplexing rate has been chosen as a trade-off between bandwidth of the system (max frequency 2 MHz) and number of tolerable channel loss in case of failure of a SQUID.

The readout electronic chain is composed of a *cold* section inside the cryostat, at the same temperature of the detectors, and a *warm* section, outside the cryostat. The entire chain is composed, going from the lowest to the highest temperature, of the LC filters and the bias resistors board, the SQUIDs boxes, the SQUID control unit and the warm electronics (see figure 12).

LC filters. The LC filters necessary to the frequency domain multiplexing are assembled on dedicated boards placed at 300 mK in close proximity to the TESs. The filters are composed of a

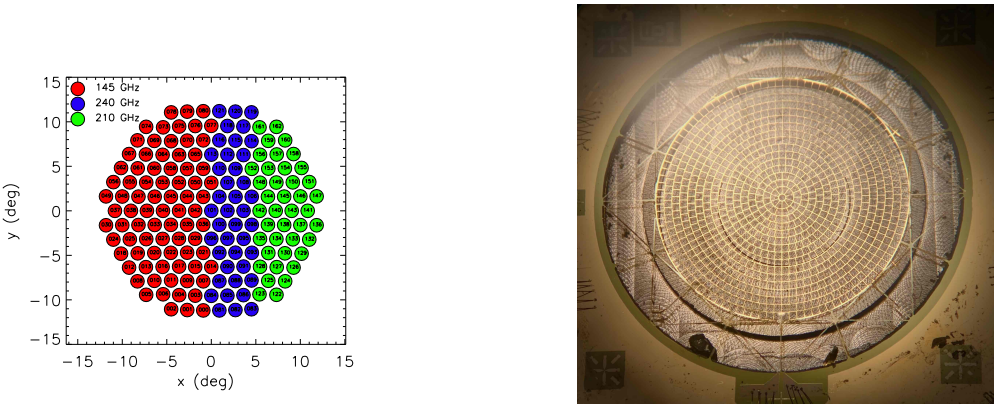

Figure 11. *Left*: distribution of detectors in one of the two equivalent focal planes. The payload rotates so that the scanning direction is along the x-axis. *Right*: a LSPE-SWIPE large spiderweb TES bolometer integrated in the backshort of the microwave cavity.

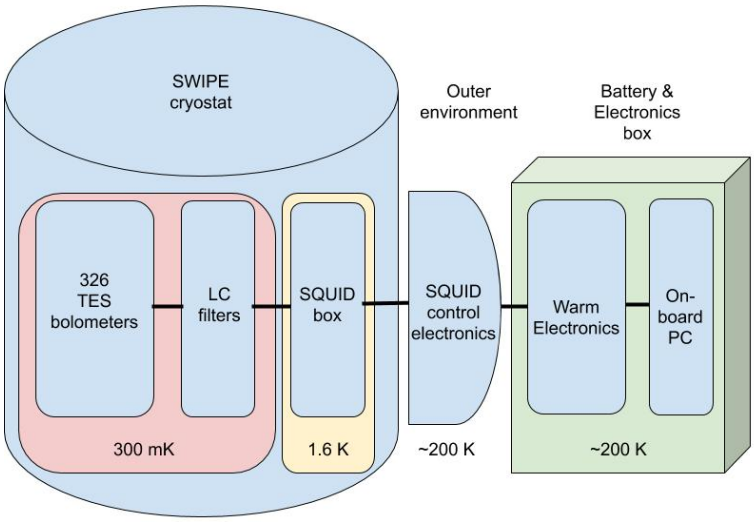

Figure 12. A scheme of the LSPE-SWIPE readout with the indication of the temperatures of the different stages.

niobium inductor fabricated by optical lithography coupled to a commercial Surface Mount Device (SMD) capacitor [67]. Given the inductance $L \approx 15\,\mu\mathrm{H}$, the capacitors are chosen in order to give resonance frequencies in the 200 kHz to 2 MHz range. Bolometers are connected to the LC board with shielded twisted pair wires. Furthermore the TES bias resistor is also placed on the board to minimize Johnson noise. Each board hosts three LC chains to read a quarter of focal plane. Four such boards are used for each focal plane for a total of eight boards.

SQUID boxes. Each LC board is connected with a custom low-inductance flat cable to a SQUID box placed at 1.6 K. Each box is used to thermalize and shield three SQUIDs, for a total of 24 SQUIDs for the two focal planes. SQUIDs convert the modulated current signal in a modulated and amplified voltage signal which in turn is sent to a further amplification stage outside the cryostat. The SQUIDs that are baselined for LSPE/SWIPE are 6-stage SQUID arrays from VTT with critical current $I_c \approx 65\,\mu\mathrm{A}$, input inductance 2 nH and a transimpedance of $30 \div 50\,\mathrm{V\,A^{-1}}$. The flux coupling and noise are $36\,\mu\mathrm{A}\,\Phi_0^{-1}$ and $\lesssim 0.1\,\mu\Phi_0\,\mathrm{Hz}^{-1/2}$ respectively (Φ_0 being the magnetic flux quantum). Two different coupling strengths can be selected for the feedback coil: $M_f^{-1} \simeq 40\,\mu\mathrm{A}\,\Phi_0^{-1}$ and $M_f^{-1} \simeq 90\,\mu\mathrm{A}\,\Phi_0^{-1}$.

SQUID Control Units. The SQUID control units (SCUs) are placed outside the cryostat and perform the main following tasks: (i) they provide the SQUID bias signal (which will be set at the SQUID operating temperature and will be tuned in flight); (ii) they linearize SQUID response by means of a flux-locked loop (FLL hereafter); and (iii) they host the amplification stage needed to amplify the SQUID output voltage before the digitizing stage. The desired amplification is achieved in two stages, in order to obtain the desired bandwidth and to minimize the noise referred at amplifier's input. The SQUID output is first amplified by a very low noise preamplifier based on a discrete JFET (IF3602) input differential cascode architecture, followed by a low noise CMOS operational amplifier (OPA301). The equivalent input noise density is $0.6\,\mathrm{nV\,Hz}^{-1/2}$ and the bandwidth extends up to at least 2 MHz [68].

Warm Readout. The warm readout boards contain the ADCs (LTM9001IV) and the DACs (LTC1668IG) that are used to generate the sum of sinusoids to bias the TES detectors and to digitize the modulated output. They in turn perform the digital demodulation and the data compression. They perform these operations by means of a system-on-module board hosting a FPGA and an ARM microprocessor (MitySOM 5CSX System-On-Module[4]). Each board, with a single FPGA-module, handles two readout chains therefore the complete readout system is composed of a total of 12 boards in a 6U standard, placed in a custom aluminum crate that provides the mechanical support and dissipates the generated heat. Each warm readout board builds the packets that are sent to the on-board computer to be assembled in one single event.

2.2.9 Observation and modulation strategy

The baseline LSPE-SWIPE observation strategy consists in continuous spinning of the payload, around the local zenith axis (spin axis), at fixed angular velocity $\omega_{\mathrm{payload}}$. This is combined with steps in telescope altitude ($90^\circ - \beta$, a few steps per day), to cover an altitude range from 35°to 55°. The Earth rotation, combined with the drift of the payload around the Arctic, ensures a slow precession of the spin axis around the Equatorial North Pole (precession axis). Precession angle α_{p} (co-latitude) and precession angular velocity ω_{Earth} are not exactly defined, due the partially random motion of the balloon, drifted by stratospheric winds. Figure 13 and table 3 show the SWIPE observation strategy and angles. In the simulations we assume that the latitude remains constant at the launching site, and that the dominant term in the precession rate is the 24 hrs Earth rotation rate, thus neglecting the wind driven term. This strategy is combined with the constant spin rate of the polarization modulator

[4] https://www.criticallink.com/product/mitysom-5csx/

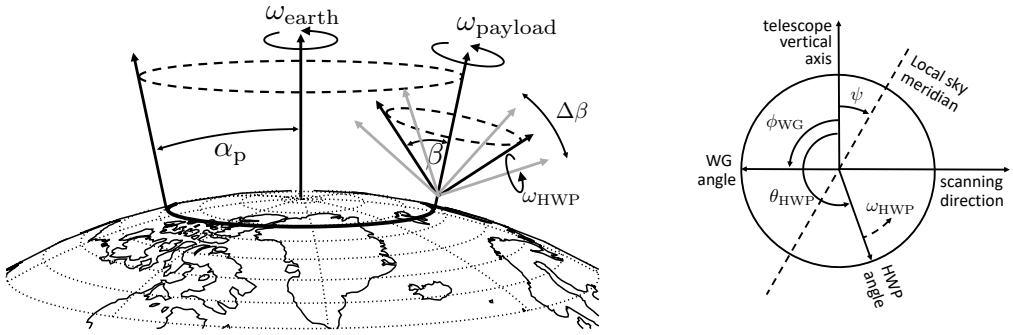

Figure 13. *Left*: LSPE-SWIPE observation strategy. The payload spin axis precesses around the North Pole, with precession angle equal to the co-latitude $\alpha_{\rm p}$, with a velocity that is a combination of the daily Earth rotation with the natural wind drift. The telescope spins around the local zenith at an angle β which can vary as $\Delta\beta$. The spin rate is reported in table 3. *Right*: LSPE-SWIPE Stokes polarimeter angles as seen from the boresight. The dashed line is the instantaneous local sky meridian; the telescope vertical axis is tilted by an angle ψ with respect to the sky meridian, and is orthogonal to the scanning direction. The wire grid inside the cryostat is oriented at an angle $\phi_{\rm WG}$ orthogonal to the vertical axis; the HWP is spinning with angular velocity $\omega_{\rm HWP}$, and forms an angle $\theta_{\rm HWP} = \omega_{\rm HWP} t$ with the telescope vertical axis.

$f_{\rm HWP}$. If the latitude remains constant, the observation covers a strip in equatorial declination δ in the range $90^\circ - (\alpha_{\rm p} + \beta_{\rm max}) < \delta < 90^\circ - (\beta_{\rm min} - \alpha_{\rm p})$ (see figure 13). The values of $\beta_{\rm min}$ and $\beta_{\rm max}$ also take into account the wide field of view $\pm 10^\circ$.

LSPE-SWIPE measures polarization with a Stokes polarimeter strategy. In an ideal case, the power hitting the detector can be computed as the first element of the Stokes vector obtained from the combination of Mueller matrices, taking into account both the rotating HWP and the WG polarizer:

$$NS_{\rm out} = M_{\rm rot}^{-1}(\phi_{\rm WG}) M_{\rm WG} M_{\rm rot}(\phi_{\rm WG}) M_{\rm rot}^{-1}(\theta_{\rm HWP}) M_{\rm HWP} M_{\rm rot}(\theta_{\rm HWP}) M_{\rm rot}(\psi) S_{\rm sky}$$

where $S_{\rm sky}$ is the Stokes vector (I, Q, U, V) of the observed direction in the sky; $M_{\rm rot}$ is the rotation Mueller matrix; $M_{\rm HWP}$ is the HWP Mueller matrix; $M_{\rm WG}$ is the WG Mueller matrix; ψ is the angle between the local meridian and the telescope vertical axis; $\theta_{\rm HWP} = \omega_{\rm HWP} t$ is the rotation angle, with respect to telescope vertical axis, of the HWP which rotates with $\omega_{\rm HWP}$ angular velocity; $\phi_{\rm WG}$ is the WG rotation angle with respect to telescope vertical axis (0° or 90° in the case of SWIPE, for reflected and transmitted radiation); and $S_{\rm out}$ is the resulting Stokes vector, of which the $I_{\rm out}$ term is the power hitting the detector. Figure 13, right panel, illustrates the angles definition. Expanding the equation, we have

$$I_{\rm out} = \frac{1}{2}\left(A I_{\rm sky}(\hat{n}(t)) + B Q_{\rm sky}(\hat{n}(t)) + C U_{\rm sky}(\hat{n}(t))\right) \tag{2.1}$$

with

$$\begin{aligned} A &= 1 \\ B &= \cos(4\omega_{\rm HWP} t + 2(\psi(t) - \phi_{\rm WG})) \\ C &= \sin(4\omega_{\rm HWP} t + 2(\psi(t) - \phi_{\rm WG})) \end{aligned}$$

where $\hat{n}(t)$ is the observed direction, and we have made explicit the time dependence.

The driving parameter to define the payload and modulator spin rate is the lowest value between detector time constant cut frequency and maximum modulation frequency. The TES developed for

LSPE-SWIPE have a typical time constant $\tau_{\rm LP} = 30\,$ms. To first approximation, this can be modelled as a single pole low-pass filter, with transfer function

$$H(\omega) = \frac{1}{1 + j\omega\tau_{\rm LP}} = \frac{1}{1 + j2\pi f\tau_{\rm LP}}, \tag{2.2}$$

(ω being the angular frequency here) with cut-off frequency $f_{\tau_{\rm LP}} = 1/(2\pi\tau_{\rm LP}) = 5.3\,$Hz. The HWP can spin up to $f_{\rm HWP} = 1.5\,$Hz, which corresponds to a modulation frequency $f_{\rm mod} = 4f_{\rm HWP} = 6\,$Hz. The limiting term is then the low pass filtering. In order to limit the sensitivity degradation due to the low-pass filtering, considering that most of the polarization signal lies in the $[3, 5]f_{\rm HWP}$ range, we set the HWP spin rate to $f_{\rm HWP} = 0.5\,$Hz. Most of the polarization signal lies then in the $[1.5, 2.5]\,$Hz range. The transfer function attenuation at $f_{\rm max} = 2.5\,$Hz is

$$|H(f_{\rm max})| = \frac{1}{\sqrt{1 + (2\pi f_{\rm max}\tau_{\rm LP})^2}} = 0.9$$

In order to set the payload angular velocity, we approximate the angular response as a Gaussian profile with standard deviation $\sigma_b = \theta_{\rm FWHM}/(2\sqrt{2\ln 2})$; given a scanning speed $\omega_{\rm payload}$, we convert the angular width into a temporal width $\sigma_t = \sigma_b/(\omega_{\rm payload}\sin\beta_{\rm max})$ where $\sin\beta_{\rm max} = 0.9$ accounts for the altitude projection effect; this can be converted into a frequency width

$$\sigma_f = \frac{1}{2\pi\sigma_t} = \frac{\omega_{\rm payload}\sin\beta_{\rm max}}{2\pi\sigma_b};$$

we require that $3\sigma_f \leq f_{\rm HWP}$, so that 99.7% of the signal lies in the $[3, 5]\,f_{\rm HWP}$ range. The condition is then:

$$3\sigma_f \leq f_{\rm HWP} \tag{2.3}$$

and the payload spin period must be:

$$T_{\rm payload} \geq 8.6\,{\rm min} \tag{2.4}$$

As a baseline, we adopt $T_{\rm payload} = 8.6\,$min. A beam FWHM is covered $N_{\rm mod}$ times the HWP modulation period, with

$$N_{\rm mod} = \frac{\theta_{\rm FWHM}}{\omega_{\rm payload}\sin\beta_{\rm max}} 4f_{\rm HWP} = 4.5$$

3 Instruments sensitivity

3.1 Instrument simulators

Simulators are key elements for instrument design and for data analysis. In the design phase, they allow to predict the scientific performance of the instruments and the impact of systematic effects. In the data analysis phase, they allow to run Monte Carlo realizations of the observations, which are necessary to estimate instrumental biases, to measure transfer functions, and to propagate uncertainties.

The instrument simulator of LSPE-Strip is written in the Julia[5] language [69] and takes advantage of Message Passing Interface (MPI) libraries to parallelize the computation. It is a modular package containing the following components:

[5] https://julialang.org/

Parameter	variable	value
Precession period	$T_{\rm Earth}$	~ 24 hrs
Precession rate	$f_{\rm Earth}$	$\sim 11.6\,\mu$Hz
Precession velocity	$\omega_{\rm Earth}$	$\sim 73\,\mu{\rm rad\,s^{-1}}$
Precession angle	$\alpha_{\rm p}$	$\sim 12 - 23^\circ$
Payload spin period	$T_{\rm payload}$	8.6 min
Payload spin rate	$f_{\rm payload}$	1.93 mHz
Payload spin velocity	$\omega_{\rm payload}$	$12.1\,{\rm mrad\,s^{-1}}$
Co-altitude	β	45°
Altitude range (combined with FOV)	$\Delta\beta$	$\pm 10^\circ \pm 10^\circ$
Max in sky speed	$\omega_{\rm payload} \sin\beta_{\rm max}$	$\sim 0.63\,^\circ\,{\rm s^{-1}}$
HWP period	$T_{\rm HWP}$	2.0 s
HWP rate	$f_{\rm HWP}$	0.5 Hz
HWP velocity	$\omega_{\rm HWP}$	$3.14\,{\rm rad\,s^{-1}}$
Modulation period	$T_{\rm mod} = T_{\rm HWP}/4$	0.5 s
Modulation rate	$f_{\rm mod} = 4 f_{\rm HWP}$	2.0 Hz
Modulations per FWHM	$N_{\rm mod}$	4.5

Table 3. LSPE-SWIPE parameters of observation and modulation strategy.

- Instrument database containing the configuration of the focal plane and the characteristics of each polarimetric chain to be integrated in the instrument;
- Pointing generation: starting from the configuration and behavior in time of the telescope motors, it produces a timestream of pointing information;
- White noise and $1/f$ noise generation;
- Destriping;
- Map-making.

Being based on a dynamic language like Julia, every module can either be called interactively in a Jupyter[6] notebook or run on a High Performance Computing (HPC) cluster.

The instrument simulator of LSPE-SWIPE consists in a parallel Fortran-90 code which takes as input:

- the number of detectors;
- the detectors position in the focal plane;
- the detectors noise, in terms of NET and $1/f$ knee frequency;
- the mission starting date and duration;
- the angular response in the sky of each detector, as a 2d matrix; this is convolved in pixel space, in a radius specified also as input parameter;
- the HWP operation strategy (stepping, spinning, spinning rate, stepping period);

[6] https://jupyter.org/

- the level of HWP synchronous systematic effects, as a signal in μK_{CMB} at the HWP spinning frequency and its harmonics;
- HWP angle offset, angular velocity instability, and error in angle measurement;
- timeline filter (high-pass, low-pass, band-pass, notch-filter);
- map-making algorithm details, as simple re-binning, or iterative destriping.

It generates in output:

- timeline of each detector;
- maps of each detector;
- map of combined detectors;
- coverage map;
- noise covariance 3×3 matrix for each observed pixel.

3.2 LSPE-Strip Noise estimation

We model the noise of the Strip polarimeters as the sum of a white noise plus a $1/f^{\alpha}$ component, so that the post-detection power spectrum can be written as:

$$P(f) = \sigma^2 \left[1 + \left(\frac{f_{\rm knee}}{f} \right)^{\alpha} \right], \tag{3.1}$$

where the knee frequency, $f_{\rm knee}$, is the frequency where the white noise and the $1/f^{\alpha}$ components contribute equally ($P(f_{\rm knee}) = 2\sigma^2$). Previous experience (QUIET, WMAP, *Planck*-LFI) shows that this simple model provides a very good first-order description of the noise properties of HEMT-based coherent devices. The standard deviation of the white noise component of the Q and U Stokes parameters measured by each Strip polarimeter in antenna temperature is given by:

$$\Delta T_{\rm r.m.s.} = \frac{1}{\sqrt{2}} \frac{T_{\rm sys}}{\sqrt{\Delta\nu\,\tau}}, \tag{3.2}$$

where $T_{\rm sys}$ is the total intensity detected by the polarimeters (sky signals, emissions from the optical components and receiver noise temperature), $\Delta\nu$ is the receiver bandwidth and τ is the integration time. The factor $1/\sqrt{2}$ in equation 3.2 results from the polarimeter correlation architecture and it is explained in [70] and section 4 of [71]. In table 4 we detail the budget leading to current estimate of the average receiver white noise performance.

We now discuss briefly the low-frequency properties of the noise spectrum and show how the expected impact from $1/f^{\alpha}$ noise components is small. In our measurements we expect two main sources of noise fluctuations on long time scales: (i) fluctuations in the receiver gain and (ii) variations in the atmospheric load. Both contribute to the $1/f^{\alpha}$ shape of the noise spectrum at low frequencies. Strip polarimeters have a very low susceptibility to gain fluctuations and $1/f^{\alpha}$ noise contributes in polarization only at frequencies less than few tens of mHz.

This stability is the result of the differential nature of the receiver that allows one to recover the Q and U Stokes parameters by differentiating signals having essentially the same intensity, thus effectively canceling out common modes. The penalty is that these detectors are practically blind

	43 GHz	95 GHz
Sky signals in antenna temperature		
Atmospheric emission at Zenith (K_{RJ})[1]	16.3	19.0
CMB (K_{RJ})	1.8	1.1
Noise contributions		
Mirror emission (K_{RJ})[2]	3.0	3.0
Window (K_{RJ})[3]	3.0	8.0
Filters (K_{RJ})[3]	2.0	3.0
Feed system (K_{RJ})[4]	0.5	0.5
Polarimeter noise (K_{RJ})[5]	34.0	104.2
System temperature[6], T_{sys} (K_{RJ})	61.7	140.0
1-second sensitivity per polarimeter[7]		
Antenna temperature $\left(\mu K_{RJ}\, s^{1/2}\right)$	514.6	1139.5
Thermod. temperature $\left(\mu K_{CMB}\, s^{1/2}\right)$	539.7	1431.4

[1]Simulated with *am* Atmospheric Model code, based on partial water vapor measurements
[2]Assumes 300 K physical temperature and 1% mirror emissivity
[3]Estimated using electromagnetic simulations (60 mm window thickness)
[4]Assumes 20 K physical temperature and ~ 0.1 dB insertion loss
[5]Measured during unit-level tests
[6]Calculated assuming a constant azimuthal distance of 20° during the whole survey.
[7]Calculated assuming the receiver bandwidth reported in table 1 and a constant azimuthal distance of 20° during the whole survey.

Table 4. White noise sensitivity budget of Strip polarimeters

to the CMB total intensity, as these measurements retain all the common-mode fluctuations and are characterized by knee frequencies of the order of several Hz.

If we assume zero or negligible polarization in the atmospheric signal we can neglect, to first order, also the effect of $1/f^{\alpha}$ fluctuations in the atmospheric load. These will contaminate polarization measurements only through any leakage from total intensity to polarization that could be present in our receivers. Provided that our current estimates indicate a leakage of the order of $\sim 0.01\%$ we believe that this effect is of second order or less.

3.3 LSPE-SWIPE noise forecast

The photon noise is computed assuming that the incoming radiation is the composition of: (i) the CMB, a 2.725 K black-body; (ii) the residual atmosphere, as computed from the *am* Atmospheric Model[7] [72] assuming a pessimistic residual ambient pressure of 10 mbar and a zenith angle of 45°; (iii) the cryostat window, as a 240 K grey-body with emissivity computed assuming a layer of Mylar [73], thickness $t = 1$ mil ($\sim 25.4\,\mu$m) with $n_r = 1.57$ and loss tangent $\tan\delta = 2.25 \times 10^{-3}$. The window emissivity is computed as $\varepsilon_{\mathrm{window},\nu} = 1 - \exp(-2\pi n_r (t/\lambda)\tan\delta)$, where λ is the wavelength [74]. Following [75], for each component, the power on the detector is computed as

$$P = \int f_\nu \eta A \Omega I_\nu d\nu \tag{3.3}$$

[7]https://doi.org/10.5281/zenodo.640645

Source	Value at source	Value at SQUID input $\left(\mathrm{pA\,Hz^{-1/2}}\right)$	Factor to SQUID input	Note	Noise on detector $\left(\mathrm{aW\,Hz^{-1/2}}\right)$
SQUID noise	$10\,\mathrm{pA\,Hz^{-1/2}}$	10	1	(a)	10
DAC LTC1668	$50\,\mathrm{pA\,Hz^{-1/2}}$	< 5	1/10	(b)	< 5
Preamplifier	$0.6\,\mathrm{nV\,Hz^{-1/2}}$	6	~ 100 V/A	(c)	6
Cabling	$0.3\,\mathrm{nV\,Hz^{-1/2}}$	3	~ 100 V/A	(d)	3
Bias resistor	$2.6\,\mathrm{pA\,Hz^{-1/2}}$	2.6	1	(e)	$\sim 2.5 - 4.0$
Total				(f)	$15 - 20$

Table 5. Contribution of selected readout electronics noise source to the NEP budget. (a) Typical noise of SQUID arrays currently being considered for the LSPE readout, given by the flux noise multiplied by the SQUID input coil coupling; (b) the DAC noise is reduced at the SQUID input by a suitable resistive divider; (c) the noise of the warm preamplifier is taken ad the SQUID input by using the SQUID transimpedence; the number reported here is the typical for the 6-series array SQUID being considered for the readout; (e) current noise of the bias resistor at 300 mK, with $R_b = 0.1\,\Omega$, and assuming the normal state resistance $R_N = 1.0\,\Omega$, and a TES resistance around $R_N/2$ in ETF; (f) assumes a TES responsivity of $-\sqrt{2}/V_{\mathrm{bias}}$ with $V_{\mathrm{bias}} \approx 1 - 2\,\mu\mathrm{V}$: the noise at squid input has to be multiplied by V_{bias} to get the NEP at detector.

where f_ν defines the filter pass-band; η is the instrument efficiency, which takes into account polarization with an extra factor 0.5; I_ν is the spectral brightness ($\mathrm{W\,m^{-2}\,sr^{-1}\,Hz^{-1}}$) of the component; $A\Omega$ is the throughput, estimated as $N_{\mathrm{modes}}\lambda^2$, with N_{modes} the number of electromagnetic modes coupled to each detector. The photon noise equivalent power in $\mathrm{W\,Hz^{-1/2}}$ of a beam filling source is computed as:

$$\mathrm{NEP}_{\mathrm{ph}}^2 = 2\int f_\nu \eta A\Omega I_\nu h\nu\left(1 + \frac{f_\nu \eta c^2 I_\nu}{h\nu^3}\right)d\nu. \tag{3.4}$$

The total photon noise $\mathrm{NEP}_{\mathrm{ph\text{-}total}}$ is the quadrature sun of the photn noise from the CMB, $\mathrm{NEP}_{\mathrm{ph\text{-}CMB}}$, the atmosphere, $\mathrm{NEP}_{\mathrm{ph\text{-}atm}}$, and the window $\mathrm{NEP}_{\mathrm{ph\text{-}window}}$. Also the thermal noise of the detector depends on the power hitting the detector. The higher the power, the higher must be the thermal conductivity G which links the detector to the thermal bath, in order to avoid transition of the TES to normal state. Following [76], the thermal noise is computed as

$$\mathrm{NEP}_{\mathrm{detector}} = \sqrt{4k_B T_c^2 GF} \tag{3.5}$$

where k_B is the Boltzmann constant, $T_c = 550\,\mathrm{mK}$ is the critical temperature, and $F = [0.5; 1]$ takes into account non-equilibrium effects in TES (we assume a pessimistic $F = 1$). The optimal thermal conductivity is

$$G = \frac{nP_{\mathrm{sat}}T_c^{n-1}}{T_c^n - T_{\mathrm{bath}}^n} \tag{3.6}$$

where $n = 3.2$ takes into account the thermal dependence of the conductivity, $T_{\mathrm{bath}} = 300\,\mathrm{mK}$ is the temperature of the thermal bath, and $P_{\mathrm{sat}} = 2.5\,P_{\mathrm{total}}$ is the saturation power, with a 2.5 safety factor (P_{total} being the total power on the detector). Given that the detectors are all built with the same characteristics, we set the detector noise (equation 3.5) using the highest value among the thermal conductivity of the 3 bands, G_{max}. With this highest value, we compute the typical detector noise, $\mathrm{NET}_{\mathrm{detector,max}}$. Combining equation 3.5 with 3.6 and 3.3, it can be noted as $\mathrm{NEP}_{\mathrm{detector}}$ is proportional to $(A\Omega)^{1/2}$.

We now discuss the contribution of the readout electronics to the instrument noise figure. We will show how the design of the electronic chain can keep this contribution below $\mathrm{NEP}_{\mathrm{readout}} <$

Band (GHz)	145	210	240
bandwidth	30%	20%	10%
$N_{\rm modes}$	[10;17]	[23;32]	[32;39]
$A\Omega\ \left(\mathrm{m^2\ sr}\right)$		$N_{\rm modes}\lambda^2$	
efficiency η	0.3	0.25	0.25
Power on cryostat entrance			
$P_{\rm CMB}$ (pW)	9.1	7.7	3.9
$P_{\rm atm}$ (pW)	0.9	1.9	9.8
$P_{\rm window}$ (pW)	1.0	2.8	2.4
$P_{\rm total}$ (pW)	11.0	12.4	16.1
Power on detector			
$P_{\rm total\text{-}detector}$ (pW)	3.3	3.1	4.0
Noise on detector			
$\mathrm{NEP_{ph\text{-}CMB}}\ \left(\mathrm{aW\ Hz^{-1/2}}\right)$	23.5	23.3	17.6
$\mathrm{NEP_{ph\text{-}atm}}\ \left(\mathrm{aW\ Hz^{-1/2}}\right)$	8.4	12.3	34.1
$\mathrm{NEP_{ph\text{-}window}}\ \left(\mathrm{aW\ Hz^{-1/2}}\right)$	7.8	14.2	13.9
$\mathrm{NEP_{ph\text{-}total}}\ \left(\mathrm{aW\ Hz^{-1/2}}\right)$	26.1	29.9	40.8
$G\ \left(\mathrm{pW\ K^{-1}}\right)$	56.1	52.7	68.4
$G_{\rm max}\ \left(\mathrm{pW\ K^{-1}}\right)$		68.4	
$\mathrm{NEP_{detector}}\ \left(\mathrm{aW\ Hz^{-1/2}}\right)$	30.6	29.7	33.8
$\mathrm{NEP_{detector,max}}\ \left(\mathrm{aW\ Hz^{-1/2}}\right)$		33.8	
$\mathrm{NEP_{readout}}\ \left(\mathrm{aW\ Hz^{-1/2}}\right)$		20	
$\mathrm{NEP_{total}}\ \left(\mathrm{aW\ Hz^{-1/2}}\right)$	47.2	49.4	56.6
Optical noise			
$\mathrm{NEP_{optical\text{-}total}}\ \left(\mathrm{aW\ Hz^{-1/2}}\right)$	157	197	226
$\mathrm{NET}\ \left(\mu\mathrm{K_{CMB}\ s^{1/2}}\right)$	11.4	12.3	26.2
margin m (%)	5	20	20
$\mathrm{NET_{eff}}\ \left(\mu\mathrm{K_{CMB}\ s^{1/2}}\right)$	12.6	15.6	31.4

Table 6. LSPE-SWIPE detectors radiative power and noise estimation. See text for details.

20 aW Hz$^{-1/2}$, in order to be sub-dominant with respect to photon noise $\mathrm{NEP}_{\mathrm{ph\text{-}total}}$ and detector thermal noise $\mathrm{NEP}_{\mathrm{detector}}$. To do so, we first refer known noise sources at the SQUID input by applying the appropriate conversion factors. We take into consideration the following noise sources: the SQUID current noise, the DAC current noise, the SQUID preamplifier noise and the Johnson noise of the cabling between the cold (inside the cryostat) and the warm (outside) section of the electronics. In table 5 we quote their typical values together with the factor needed for comparison at the SQUID input. See [77] for further details on the assumed noise model.

The total readout current noise is computed as the quadrature sum of these contributions and it is translated to a readout noise equivalent power, $\mathrm{NEP}_{\mathrm{readout}}$, by means of the TES current responsivity, R_I. To do so, we take into account the low frequency limit of R_I in strong electro-thermal feedback condition, i.e. $R_I \simeq -\sqrt{2}/V_{\mathrm{bias}}$, where V_{bias} is the TES bias voltage, and the $\sqrt{2}$ factor originates from the AC bias in the multiplexing scheme (see the discussion in the appendix of [78] for further details). The number quoted in table 5 is obtained assuming the expected voltage bias of $V_{\mathrm{bias}} \approx 1 - 2\,\mu\mathrm{V}$.

The total noise equivalent power, $\mathrm{NEP}_{\mathrm{total}}$, is computed by quadrature sum of the photon noise from different sources, the detector thermal noise and the readout noise. The optical noise, which converts the noise on the detector to noise at the instrument aperture, taking efficiency into account, is computed as

$$\mathrm{NEP}_{\mathrm{optical\text{-}total}} = \mathrm{NEP}_{\mathrm{total}}/\eta$$

Results of this calculation is converted to $\mu\mathrm{K}_{\mathrm{CMB}}\,\mathrm{s}^{1/2}$ as:

$$\mathrm{NET} = \frac{T_{\mathrm{CMB}}}{\int f_\nu A\Omega B(T_{\mathrm{CMB}}) \frac{xe^x}{e^x-1} dx} \frac{\mathrm{NEP}_{\mathrm{optical\text{-}total}}}{\sqrt{2}} \tag{3.7}$$

where $B(T_{\mathrm{CMB}})$ is the CMB black-body brightness, $x = h\nu/(k_B T_{\mathrm{CMB}})$ is the reduced frequency, and the factor $1/\sqrt{2}$ takes into account the conversion from $\mu\mathrm{K}_{\mathrm{CMB}}\,\mathrm{Hz}^{-1/2}$ to $\mu\mathrm{K}_{\mathrm{CMB}}\,\mathrm{s}^{1/2}$. Notably, the photon noise NEP (as the thermal noise) is proportional to $(A\Omega)^{1/2}$, while the NET is inverse proportional to $(A\Omega)^{1/2}$ and thus to $N_{\mathrm{modes}}^{1/2}$. This is the advantage of multi-moded detectors: higher photon noise, which relaxes detector noise requirement, and lower NET. Background and noise calculation results are reported in table 6. In order to take into account possible effects such as contamination by cosmic rays (see next section), atmospheric background variation, detectors yield, detector excess noise, and other unexpected effect, we also report the margin m value and the effective noise,

$$\mathrm{NET}_{\mathrm{eff}} = \mathrm{NET}(1 + m),$$

which we use as input in the instrument simulator, for the results reported in section 5. The margin m is not the same for all channels, due to the largest uncertainty in the atmospheric modelling in the highest frequencies.

3.3.1 Cosmic rays rate

TES detectors are sensitive to any form of energy deposited on the absorber, including the effect of cosmic rays. The flux of primary cosmic rays in the upper atmosphere is fairly well known, as well as its dependence on the latitude and on the solar cycles. We evaluated the expected rate of interactions by cosmic rays in the upper atmosphere (altitude 40 km) along the orbit of SWIPE by using the measured fluxes and simulating the interactions of primary protons and alphas on the SWIPE cryostat, instrument and focal plane. An energy-integrated flux of 1.5 particles $\mathrm{cm}^{-2}\,\mathrm{s}^{-1}$ is obtained at the minimum of the solar activity cycle, decreasing by a factor ≈ 2.5 at the solar activity maximum.

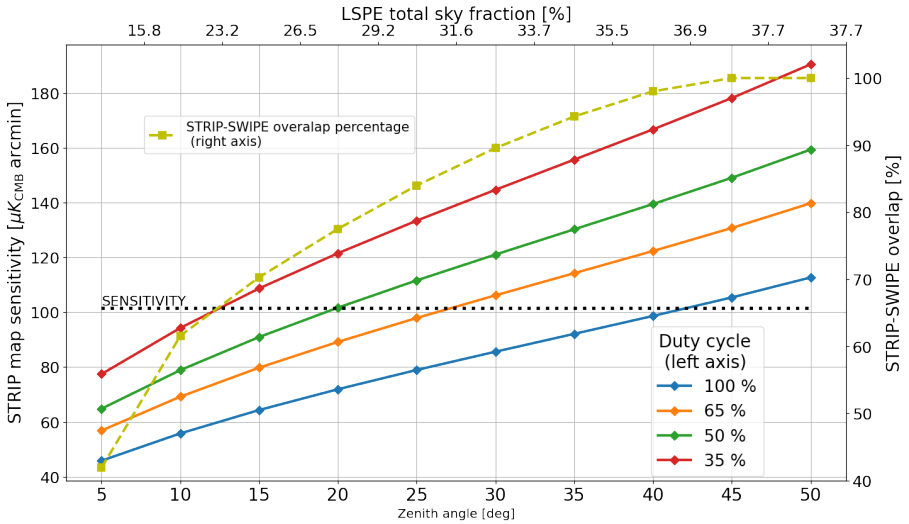

Figure 14. LSPE-Strip map sensitivity as a function of the zenith angle and of the fraction of usable duty cycle (left axis). The black-dotted line (left axis) represents the value of the map sensitivity as reported in table 1. The dashed gold line shows the Strip-SWIPE overlap percentage (right axis). The top axis reports the corresponding cumulative sky fractions.

We assume that cosmic rays release a signal in the bolometers whenever they interact with the gold-plated spiderweb structure. By using the geometrical characteristics of our spiderweb bolometers (diameter 8 mm, fill factor 8%) we estimate an interaction rate of 60 mHz per bolometer, giving roughly a 1 Hz rate of interaction per readout chain, being the bolometers multiplexed in groups of 16. The 60 mHz rate is reasonable once compared with the (inverse of the) bolometer time constant, nevertheless suitable algorithms for cosmic ray hit identification and removal must be implemented. These algorithms also subtract the long tail after the glitch in the data. In a typical case, after a glitch, it is impossible to recover the first part of the tail, equal to $[5; 10]\,\tau_{\rm LP}$. With a rate of one event every 16.7 s and a time constant $\tau_{\rm LP} = 30$ ms, this correspond to removing between 1 and 2% of the data, well within our margins.

3.4 Sky coverage

LSPE-SWIPE is expected to have a fixed sky coverage of about 38% of the Northern Sky, with the precise values depending on the choice of the launching station. On the other hand, the sky fraction observed by LSPE-Strip can be adjusted by changing the telescope elevation [79], resulting in different sensitivity per sky pixel at the end of the survey. The final Strip strategy will be defined to trade-off the sky coverage with the noise per pixel distribution and to maximize the overlap between the sky regions observed by the two LSPE instruments.

The baseline configuration of the Strip observation strategy assumes a constant zenith angle of 20°. Such configuration yields a map average noise $\sigma_{Q,U} = 102\,\mu$K arcmin in each 1° pixel. Assuming two years of observation time, we can calculate the sensitivity with respect to this baseline value as a function of the zenith angle and of the usable fraction of time (duty cycle). This is shown in figure 14 together with the percentage of overlap, and the total sky fraction as a function of the zenith angle.

In the analysis reported in this paper, we assume a standard coverage for SWIPE, with a launch from Longyearbyen. In this case, the optimal overlap is obtained with a Strip zenith angle of 35°,

resulting in the coverage shown in figure 1. The map noise is then $\sigma_{Q,U} = 120\,\mu\mathrm{K}\,\mathrm{arcmin}$, with a wider coverage, providing the best trade-off for final results reported in sections 5.

4 Systematic effects and calibration

In this section we present the most relevant systematic effects for the two instruments, with particular focus on the systematic effects critical for the measurement of the CMB polarization. We also set requirements on the knowledge of the most important instrumental parameters, and discuss the calibration plans.

4.1 LSPE-Strip systematic effects

Here we provide a brief summary of the Strip susceptibility to systematic effects, deferring to forthcoming papers a more detailed treatment. We start by listing the following sources of systematic effects:

- non-perfect behavior in the polarimetric receiver chain;
- thermal and/or electrical fluctuations;
- fluctuations in the atmosphere;
- straylight from astrophysical and non-astrophysical sources (Galactic emission, ground emission pickup, shields, etc.);
- optical imperfections (e.g., main beam asymmetry);
- imperfect pointing;
- imperfect calibration (photometric, beam and polarization angle).

Polarimetric effects. Strip polarimeters are based on the QUIET design providing significant advantage: (i) the Q and U Stokes parameters are measured directly for each horn in the focal plane, instead of being recovered through the inversion of a condition matrix, (ii) the system is unaffected by gain and bandpass mismatches between the two acquisition lines of the same polarimeter, as well by as unbalances in phase switch states, and (iii) $1/f$ noise and other common-mode effects are efficiently removed from Q/U timelines thanks to double demodulation.

The most important polarization effect in the polarimetric chain is caused by the cross-polarization in the polarizer-OMT assembly, that causes a leakage from total intensity to polarization. We have already reported, in section 2.1.4, that the Strip polarizer-OMT assembly displays a cross-polarization level of $\lesssim -30\,\mathrm{dB}$, which ensures an overall $I \rightarrow Q/U$ leakage less than 0.01%.

Another possible source of systematic effects is the difference in the bandpass among the various polarimeters. In fact, the polarimeters average the incoming signal over the bandpass, so that if the bandpasses are different and the source is not a black-body (as it contains, for example, the Galactic synchrotron emission) we have a residual systematic effect in the final, averaged map. We have performed simulations using bandpasses measured in the laboratory, a synthetic sky with CMB, Galactic synchrotron and dust emissions, and Monte Carlo realizations of the instrumental noise. Our results show that the angular power spectrum of the residual effect in polarization is about three orders of magnitude below the noise level, so that we can neglect it.

Other imperfections are either compensated for by design (e.g. gain unbalance), or generate a leakage between U and Q that we estimate to be $\lesssim 1\%$ on the basis of the measured and simulated parameters of the various components in the polarimetric chain.

Parameter	Description	Units
TQI	Total precipitable ice water	$\mathrm{kg\,m^{-2}}$
TQL	Total precipitable liquid water	$\mathrm{kg\,m^{-2}}$
TQV	Total precipitable water vapor	$\mathrm{kg\,m^{-2}}$
QVM10	10-meter specific humidity	$\mathrm{kg\,kg^{-1}}$
PS	Surface pressure	Pa
TS	Surface skin temperature	K
T10M	10-meter air temperature	K
U10M	10-meter eastward wind	$\mathrm{m\,s^{-1}}$
V10M	10-meter northward wind	$\mathrm{m\,s^{-1}}$

Table 7. Physical parameters of the atmosphere considered in our simulations.

Thermal/electrical fluctuations. Variations in temperature and bias voltages will generate common-mode fluctuations in the total intensity signal that will be canceled by the double demodulation. Only temperature variations in the feedhorn-OMT system can, in principle, leave a small residual in the Q and U parameters because of the leakage from intensity to polarization caused by the front-end cross-polarization. This residual effect is expected to be negligible and we will control its impact during data analysis by exploiting the instrument temperature housekeeping data.

Fluctuations in the atmosphere. The atmosphere impacts CMB polarization measurements from the ground in two ways: (i) its average brightness temperature increases the noise level of the measurements and (ii) it is a source of low-frequency noise in the data because of brightness temperature fluctuations.

Regarding the atmospheric load we have estimated an average brightness temperature of 16.3 K at 43 GHz and 19.0 K at 95 GHz (see table 4). The estimate is based on simulations carried out with the *am* Atmosferic Model code using precipitable water vapor (PWV) measurements collected during 2018.

Brightness temperature fluctuations in the atmosphere are caused by PWV variations that follow the typical sub-tropical seasonal modulation. The effect of these fluctuations are canceled to first order in the polarization data by the pseudo correlation architecture of the Strip polarimeters. A small fraction of these intensity fluctuations, however, leaks into Q and U because of the non-zero cross polarization of the polarizer-OMT assembly. Although this fraction is small ($\sim 0.01\%$) we are developing a Monte Carlo simulations to estimate their impact on polarization measurements.

The simulations use data provided by the MERRA-2[8] reanalysis to construct cumulative distribution functions (CDF) of the relevant physical atmospheric parameters. We then use our simulation-framework, `Stripeline`[9], to estimate the contribution of the seasonal atmospheric fluctuations.

In table 7 we list the atmospheric physical parameters used in our simulations, while in figure 15 we show an example of the cumulative PWV distribution in Tenerife from 1980 – 2019 derived from MERRA-2 reanalysis.

Straylight. We define straylight the overall signal detected by the instrument from directions outside the main beam. The origin of these signals, detected by the optics sidelobes, can be astrophysical

[8] https://disc.gsfc.nasa.gov/
[9] https://github.com/lspestrip/Stripeline.jl

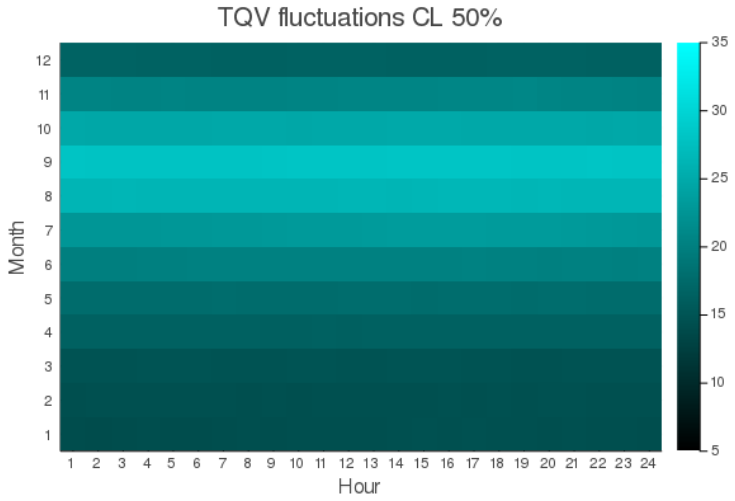

Figure 15. Daily and seasonal fluctuations of the PWV above Pico del Teide - Tenerife. We can appreciate the quite stable daily PWV fluctuations compared to the seasonal ones. The color-scale is in kg m^{-2} units.

(e.g. the Galaxy), terrestrial (the emissions from the ground) and instrumental (e.g. the emissions from the telescope enclosure shields).

The sidelobes can contribute to a spurious polarization in two ways: (i) by detecting directly a polarized signal far from the main beam (from the sky, from the Earth and from the Sun) and (ii) by converting a total intensity emission to polarization due to the cross-polar response of the optical system.

Regarding the first point, our preliminary estimates based on the simulated beam far sidelobes show that spurious polarization detected directly from the sky is less than $\sim$ 3 nK and, therefore, negligible. The assessment of the polarized input from the Earth is more difficult, because of the lack of data on the polarization properties of the microwave Earth emissions. Using Earth brightness temperature data measured at 37 GHz by the Special Sensor Microwave/Imager instrument on board the Defense Meteorological Satellite Program[10] we estimated an upper limit of 0.1 K of polarized emission from the Earth potentially entering the telescope far sidelobes. We also estimated that with the current shielding this contribution should be maintained below $\sim$ 0.05 μK in the scientific data.

To avoid Sun contamination during daytime we will discard data where the Sun is at an angular distance less than 10° from the telescope line-of-sight. Our simulations show that this fraction corresponds to about 15% of the data and is included in our duty cycle computation. When the Sun is farther than 10° its emission will be detected by the beam far sidelobes that are at the level of about −100 dB, enough to dilute this signal to negligible levels.

Regarding the intensity-to-polarization leakage we have considered the input from the sky and from temperature variations in the optical enclosure. Considering the 44 GHz *Planck* sky maps combined with the instrument cross-polarization upper limits we find that the sky contributes with a spurious polarization of $\sim$ 0.01 μK. The polarization systematic effect induced by optical enclosure temperature fluctuations is not a concern, provided that we will be able to measure and decorrelate these fluctuations from the data.

[10] http://www.remss.com/missions/ssmi

Main beam asymmetry. Asymmetry in the main beams is a source of leakage from intensity to polarization that can be corrected in the power spectra, provided that one knows the main beams with percent precision down to about −25 dB. In Strip we further control this effect "in hardware", thanks to the very symmetric optical response of the telescope crossed-Dragonian design that guarantees an average beam ellipticity less than 1% with a corresponding cross-polar discrimination better than −40 dB.

Pointing effects. Strip will implement a night optical star tracker that will allow us to reconstruct the pointing with a precision of 15′′ or better, that will allow us to neglect pointing systematic effects.

As a reference, the precision reached by *Planck* for the 44 GHz LFI channel was 27′′ for the pointing reconstructed from the nominal Jupiter scans and 19′′ for the pointing reconstructed from the deep Jupiter scans [80, section 5.3]. This precision was enough to guarantee the scientific performance and the impact of errors in the pointing reconstruction could be considered negligible [81, figure 8].

Calibration effects. An important source of systematic effects is the uncertainty in the instrument calibration parameters: (i) the photometric calibration (also named "responsivity") that converts the raw time-ordered-data into brightness temperature units, (ii) the beam pattern and (iii) the polarization angle, that defines the reference frame in which Q and U are measured by the polarimeters. We summarize our calibration strategies in section. 4.2. To first order we will manage calibration effects "in-hardware", i.e., by achieving high precision in the measurement of the instrument calibration parameters. We will measure the photometric constant with a relative precision better than 1% exploiting a combination of natural and artificial sources, and the main beams down to −25 dB with an r.m.s. precision better than 1% using a source placed on an Unmanned Aerial Vehicle (UAV). The polarization angle is known from the mechanical disposition of the feedhorns in the focal plane and its uncertainty is limited by mechanical tolerances and thermo-elastic variations during cooldown. Previous experience with *Planck*-LFI [82, section 2.1.3] show that these uncertainty is less than 0.5°. In figure 16 [adapted from 83] we show our estimate of the impact of photometric calibration and polarization angle uncertainty on the power spectra measured by Strip. The colored areas highlight the effect of ±10% uncertainty in the photometric calibration (a highly conservative estimate), while the bundle of purple and green lines is the result of a Monte Carlo simulation of a ±1° uncertainty in the polarization angle.

4.2 LSPE-Strip calibration

We briefly describe here how we will measure the three main instrumental calibration parameters: (i) the photometric constant, (ii) the beam pattern and (iii) the polarization angle.

Photometric calibration. We distinguish here two steps in the determination of the photometric constant: (i) "absolute calibration", i.e. the determination of the absolute value of the photometric constant and, (ii) "relative calibration", the measurement of time variations in the instrument responsivity caused by gain fluctuations.

Because the architecture of the Strip polarimeters does not allow stable measurements in total intensity, for absolute calibration we must rely on bright polarized sources with known flux. The Crab Nebula is undoubtedly the best flux calibrator at these frequencies and we have shown that with one day of data it is possible to achieve a precision $\lesssim 10\%$, while few weeks will be enough to approach a precision of $2-3\%$ [84].

Regarding relative calibration, we will measure instrumental gain changes with a stable signal generated by two thermally stabilized microwave generators (one in Q-band and the other in W-

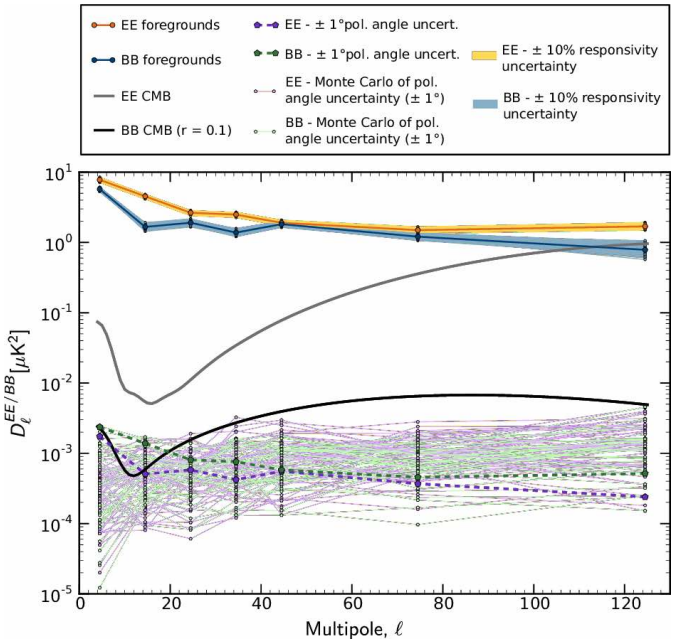

Figure 16. Power spectra evaluating the impact of polarization angle and photometric calibration uncertainty on Strip measurements.

band) installed in the optical assembly. Fluctuations currently measured in our laboratory are less than 0.2%, which will allow us to achieve a relative calibration with an overall precision better than 1%.

Beam calibration. The presence of $1/f$ noise in the total intensity data measured by Strip limits our ability to exploit natural point-sources, like Jupiter, to calibrate the main beams. Therefore, we have developed an artificial calibrator system based on a microwave source placed on an UAV [85] that will fly over the Strip telescope during the commissioning campaign, and will allow us to measure the main beams with the required precision (1% at −25 dB).

Polarization angle. The Strip polarimeters measure directly the Stokes parameters Q and U in a coordinate system defined by the mechanical layout of the polarizer-OMT assembly [24] and, ultimately, by the orientation of the OMT output waveguides. This means that the knowledge of the polarization angle is determined by the mechanical design and limited to about 0.5° by mechanical tolerances and by possible thermoelastic variations during cooldown.

4.3 LSPE-SWIPE systematic effects and calibration

LSPE-SWIPE is designed to minimize instrumental polarization. This is the spurious signal resulting from the measurement of unpolarized radiation. In the case of CMB, the amount of unpolarized radiation coming from the sky is overwhelming with respect to the polarized signal, minimizing instrumental polarization is the most important driver of instrument design. The requirement is that the maximum acceptable level of instrumental polarization is 0.04%. In this way we will get a constant polarized signal lower than 1 mK from the unpolarized background, while from CMB anisotropy we will get at most 0.2 μK spurious polarization, correlated to temperature fluctuations (even less at large angular scales). This instrumental polarization is generated by the cryostat window, due to the effect

of incident radiation not orthogonal to the window surface, in particular in the case of off-axis detectors. The constant signal is treated as an offset in the data analysis, whose stability depends on the stability of the gain of the electronics and of the responsivity of the detectors, and is not synchronous with the observed sky. Instrumental polarization is reduced during system design using an optical system close to on-axis, and avoiding mirrors in favor of lenses. The main design choice here is to have the polarization modulator as the first optical elements in the system, thus relaxing significantly the requirements on the following optical components.

The second parameter to be considered is cross-polarization. Cross-polarization is defined as the response of a polarimeter to an input signal polarized in direction orthogonal to the nominal polarimeter direction. Cross-polarization results in leakage of E-modes into B-modes. Our requirement is that the maximum acceptable level of cross-polarization is below 2%. This is achieved again by means of an accurate optical design.

The third parameter to be considered is the ellipticity of the main beam (detector angular response in the sky). Spinning of the Half-Wave Plate allows to observe the same sky region with the same beam orientation, and different polarimeter orientation. This strongly mitigates the ellipticity requirement, and differential ellipticity among different detectors.

Correct measurement of the angles of the polarimeters is crucial to avoid leakage from E-modes into B-modes, and to avoid contamination in the measurement of fundamental physics effects such as cosmic birifringence. In this context, our system is characterized by the presence of a single, large wire grid polarizer, defining the reference system for polarization measurements. With this design the system is similar to an ideal polarimeter, and the angle of the single large wire grid polarimeter can be accurately measured. The requirement on the polarimeter angle mesurement is set in the next section.

Spectral matching among detectors has been historically a problem for instruments without a polarization modulator, just comparing two independent measurements of the orthogonal polarization components. In LSPE-SWIPE we use a Stokes polarimeter, where the same detector measures both polarizations, alternated by means of a rotating half-wave plate. In this configuration the most important requirement is that the waveplate has high modulation efficiency over the detection bandwidth of the focal plane it serves. In our system a single waveplate covers all the bands from 120 to 260 GHz. This requires over 70% bandwidth for the waveplate, a goal certainly reachable with significant accuracy, by means of metamaterials [see 86].

4.3.1 Polarization angles and detectors time response requirements

One of most problematic systematic effects for any B-modes probe is the the presence of a systematic error $\Delta\alpha$ in the polarization angle reconstruction. Such an error induces a Q to U rotation, and a E, B-modes leakage [87]:

$$\begin{cases} C_\ell^{EE,obs} = C_\ell^{EE}\cos^2(2\Delta\alpha) + C_\ell^{BB}\sin^2(2\Delta\alpha) \\ C_\ell^{BB,obs} = C_\ell^{BB}\cos^2(2\Delta\alpha) + C_\ell^{EE}\sin^2(2\Delta\alpha). \end{cases} \tag{4.1}$$

In order to set the requirement on the knowledge of SWIPE wire grid and polarization angle, we have run an estimation of the likelihood of r, as described in section 5.2, for a sky with a rotation of the E, B space as in equation 4.1. The result is reported in figure 17, in terms of a bias in r, if the recovered polarization is rotated by a given angle. In the case of LSPE-SWIPE the rotation may be due to a rotation of the Wire Grid, by an angle $\Delta\phi_{\rm WG}$ or by a rotation of the Half-Wave Plate, by an angle

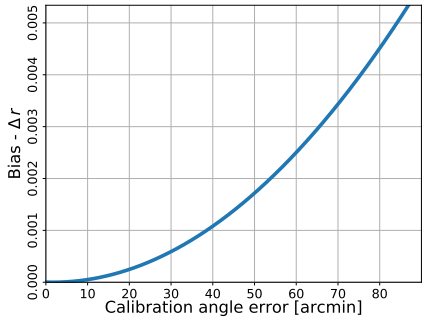

Figure 17. Bias in r due to a rotation in the polarization angles.

$2\Delta\Theta_{\rm HWP}$. From figure 17, we can set the requirements:

$$\begin{aligned} \Delta\phi_{\rm WG} &< 40'/\sqrt{2} = 28' \\ \Delta\theta_{\rm HWP} &< 20'/\sqrt{2} = 14' \end{aligned} \tag{4.2}$$

so that the uncorrelated combination of the two errors is $\Delta\alpha = 40'$, which produces a bias $\Delta r \sim 0.001$, corresponding to 10% of the uncertainty in r. These requirements are valid for the angles knowledge, in the case this is the only uncertainty in the system. In section 4.3.2 we consider the combination of a number of systematic effects, relevant for the measurement of the polarization. With that joint analysis, we set more stringent requirements as reported in table 8.

The TES detectors of SWIPE have an intrinsic time response. Their temporal transfer function $H(\omega)$ can be approximated by a single pole low pass filter, as in equation 2.2. More precisely, the time transfer function is characterized by an amplitude, $|H|$ (gain effect) and a phase $\Phi(H)$ (time delay effect). The time delay is

$$\Delta t = \frac{\Phi(H)}{2\pi} T = \frac{\Phi(H)}{\omega},$$

where $\omega = 2\pi f$ is the signal angular frequency of interest, 3 to $5\omega_{\rm HWP}$ in our case. During this time, the HWP moves of an angle

$$\Delta\theta_{\rm HWP} = \omega_{\rm HWP}\Delta t = \Phi(H)\frac{\omega_{\rm HWP}}{\omega}.$$

This time delay is deconvolved in the analysis pipeline. An error in the knowledge of the transfer function phase has the same effect of an error on the knowledge of the HWP angle. Given the requirement on the HWP angle knowledge, $\Delta\theta_{\rm HWP}$, we can set the requirement on the knowledge of the transfer function phase as:

$$\sigma_\Phi = \frac{\omega}{\omega_{\rm HWP}}\Delta\theta_{\rm HWP} = 3\Delta\theta_{\rm HWP} = 42' = 12\times10^{-3}\,\text{rad} \tag{4.3}$$

where we have considered that the frequencies of interest range from $3f_{\rm HWP}$. We can express this requirement in terms of the level of knowledge of the time constant $\tau_{\rm LP}$ of a single pole low-pass filter, considering that $\tan\Phi = -\omega\tau_{\rm LP}$. An error on the time constant $\sigma_{\tau_{\rm LP}}$ generates an error on the phase

$$\sigma_\Phi = \frac{\omega}{(\omega\tau_{\rm LP})^2+1}\sigma_{\tau_{\rm LP}}.$$

Inverting

$$\sigma_{\tau_{\rm LP}} = \frac{(\omega\tau_{\rm LP})^2+1}{\omega}\sigma_\Phi = \frac{(\omega\tau_{\rm LP})^2+1}{\omega_{\rm HWP}}\Delta\theta_{\rm HWP},$$

where we have used equation 4.3. With a time constant $\tau_{\rm LP} = 30\,$ms and a frequency in the 1.5 to 2.5 Hz range, this means a requirement:

$$\sigma_{\tau_{\rm LP}} \simeq 1.5\,{\rm ms} \tag{4.4}$$

(relative error $\sigma_{\tau_{\rm LP}}/\tau_{\rm LP} = 5\%$). Also in this case, the requirement will be more stringent if considered jointly with other effects.

The HWP angle error and the error on the phase of the time transfer function can be disentangled and calibrated by spinning the HWP at different angular velocities, or different directions, both in flight and on the ground, in calibration phase.

4.3.2 HWP synchronous systematic effects and mitigation

Besides errors in the polarization angle reconstruction, discussed in the previous section, another critical contamination in HWP based polarimeters is the generation of spurious signals at the frequency of the plate rotation, or its harmonics. Small differences ($\sim 10^{-3}$) in the absorption coefficients along the ordinary and extraordinary axes of the HWP produce a polarized emission. This radiation is modulated at twice the HWP spin frequency, $2f_{\rm HWP}$, when is transmitted by the polarizer but could also be reflected by the polarizer, and back by the HWP, and induce a spurious signal at $4f_{\rm HWP}$, the same frequency as the sky polarized signal [88]. By simulations, the $2f_{\rm HWP}$ contribution produces an equivalent temperature fluctuation of $\sim 1 - 10\,{\rm mK_{CMB}}$ while the $4f_{\rm HWP}$ contribution is $< 5\,\mu{\rm K_{CMB}}$ if the HWP temperature is kept below 10 K. This last term is completely negligible in comparison to the instrumental polarization requirement set at 0.04%, corresponding to a polarization signal of 1 mK. These spurious signals must be removed by dedicated data analysis techniques.

For the case of SWIPE, we developed a specific pipeline to deal with any spurious term synchronous with the HWP spin frequency, or harmonics. This is based on application of notch filters, at the frequencies of interest, and an iterative map-making to recover the removed signal. The notch filters are designed as

$$F(f) = \begin{cases} 1 & \text{if } f < f_1 \\ 0.5\left(1 + \cos\left(\pi \frac{f-f_1}{f_2-f_1}\right)\right) & \text{if } f_1 < f < f_2 \\ 0 & \text{if } f_2 < f < f_3 \\ 0.5\left(1 - \cos\left(\pi \frac{f-f_3}{f_4-f_3}\right)\right) & \text{if } f_3 < f < f_4 \\ 1 & \text{if } f > f_4 \end{cases} \tag{4.5}$$

where $f_1 = f_0 - 2\Delta f$, $f_2 = f_0 - \Delta f$, $f_3 = f_0 + \Delta f$, and $f_4 = f_0 + 2\Delta f$ are the frequencies where the filter starts to drop, reaches 0, starts to rise, reaches 1 respectively; f_0 is the notch filter frequency, and Δf is the notch filter width. In simulations, we set f_0 to the HWP spin frequency and harmonics, and $\Delta f = 1\,$mHz, lower than the payload default spin rate, set at 1.93 mHz (table 3). The notch filter applied at 4 times the HWP spin rate, $4f_{\rm HWP}$ can remove some signal at the largest scales in the sky. This happens despite the payload spin rate is above the notch filter width, given that the sky signal is not exactly periodic, and part of the sky signal is spread below the spin rate frequency. This signal is recovered by an iterative mapmaking process. In the following, P is the pointing matrix, M_P is the rebinning matrix; $\otimes$ means a filtering. The iterative procedure is applied to the timeline d_j of the j-th detector:

- each timeline is notch-filtered to remove the contamination $\tilde{d}_j = F \otimes d_j$;
- all filtered timelines are combined in a first map, by simple rebin $m_0 = \sum_j M_P \tilde{d}_j$;

- here starts the iteration, from $i = 0$;
- a synthetic timeline is produced for each detector: $h_j = Pm_i$;
- the synthetic timeline is filtered by $1 - F$, to recover the missing signal: $\tilde{h}_{j,i} = (1 - F) \otimes h_{j,i}$;
- the filtered synthetic timeline is added to the filtered original timeline: $d_{j,i} = \tilde{d}_j + \tilde{h}_{j,i}$;
- a new map is produced: $m_{i+1} = \sum_j M_P \tilde{d}_{j,i}$, and the procedure is iterated.

Testing different numbers of iterations, we have found that 50 iterations represents a good trade-off between computational time and residual signal in the map with filtered timelines. Simulations have been performed with a multi-notch filter, i.e. a chain of notch filters, each with different central frequency. The payload rotation period is set to 8.6 min in accordance with equation 2.4 and the notch filters width is set to $\Delta f = 1$ mHz. Half-wave plate synchronous systematic effects are introduced at $1f_{\rm HWP}$, $2f_{\rm HWP}$,$3f_{\rm HWP}$, $4f_{\rm HWP}$ and $5f_{\rm HWP}$ with amplitude 10 mK, 10 mK, 1 mK, 1 mK and 1 mK respectively. The same frequencies are used as centers of a stack of 5 notch filters.

In order to have a more realistic simulation, these contamination have been also combined with:

- an **error in the measurement of the HWP angle**. This is defined by the uncertainty with which we can readout the HWP angle. This is described by the parameter $\sigma_{\theta_{\rm HWP}}$. We have explored $\sigma_{\theta_{\rm HWP}} = [0, 3, 10]\,'$. Our measurement precision, with Kalman filter approach, is of order $\sigma_{\theta_{\rm HWP}} \leq 0.1'$;
- an **offset in the knowledge of the HWP angle**. This is described by the parameter $\Delta\theta_{\rm HWP}$. We explored the values $\Delta\theta_{\rm HWP} = [0, 3, 10]\,'$;
- an **instability in the HWP rotation rate**, modelled as a noise in the angular velocity of the HWP. This is described in terms of relative error by the parameter $\sigma_{\omega_{\rm HWP}}/\omega_{\rm HWP}$. The angular velocity samples are simulated as

$$\omega_i = \omega_{HWP}\left(1 + \frac{\sigma_{\omega_{\rm HWP}}}{\omega_{\rm HWP}} n_i \sqrt{\frac{f_{\rm sampling}}{f_{\rm HWP}/{\rm dpt}}}\right) \tag{4.6}$$

  where n_i is a sample of a normal distributed random number, $f_{\rm sampling}$ is the simulation sampling rate, $f_{\rm HWP}$ is the HWP rotation frequency, and dpt = 64 is the number of angle measures of the HWP in a turn. $f_{\rm sampling}/(f_{\rm HWP}/{\rm dpt})$ is the number of simulated samples between two subsequent HWP measured positions. The simulation with equation 4.6 results is the same angular drift between two HWP measures, independently of the sampling rate of the simulation. We explored the values $\sigma_{\omega_{\rm HWP}}/\omega_{\rm HWP} = [0, 0.6{\times}10^{-8}, 0.6{\times}10^{-7}, 0.6{\times}10^{-6}, 0.6{\times}10^{-5}]$. Using a Kalman filter, we have measured a precision in the determination of the HWP angular velocity of order $\sigma_{\omega_{\rm HWP}}/\omega_{\rm HWP} = 2 \times 10^{-6}$.

The major contribution from HWP spin rate instability is due to the fact that the various HWP synchronous effects are not at a single frequency anymore, but are spread in frequency due to the instability, thus reducing the efficacy of the notch filter; this is partially compensated by measuring this instability, and filtering in angle domain instead than in time domain, but with some limitation coming from the uncertainty in the angular velocity measure, $\sigma_{\omega_{\rm HWP}}/\omega_{\rm HWP}$.

Figure 18 illustrates the Fourier transform of a 16 hrs noise-free SWIPE timeline, for simulations of CMB and systematic effects. In particular, the black curve represent the Fourier transform of

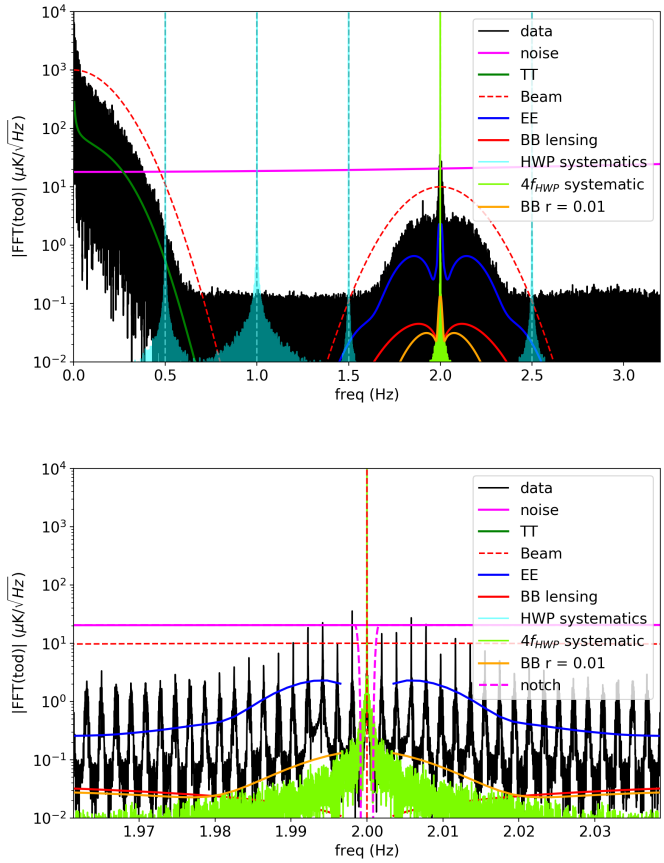

Figure 18. LSPE-SWIPE timeline in Fourier space (*top*), and zoom-in near modulation frequency (*bottom*), for a 16 hours noise-free SWIPE timeline, in case of a CMB only simulation. The bottom plot is a zoom near the polarization modulation frequency. The black curve are the data; CMB temperature data are centered around 0 frequency, and polarization data around $4f_{\rm HWP}$. The magenta line is is the noise for a single detector at 145 GHz. The magenta dashed line, is the noise multiplied by the notch filter. Vertical dashed lines represent harmonics of the HWP spin frequency. The dark green curve is the expected signal for a temperature CMB angular power spectrum, blue curve for E-modes power spectrum, red for B-modes (tensor only) and orange for inflationary B-modes. The light-green curve, visible in the bottom plot, is a systematic effect at $4f_{\rm HWP}$, with an amplitude of 1 mK, spread in frequency due to the uncertainty in the HWP angular velocity $\sigma_{\omega_{\rm HWP}}/\omega_{\rm HWP} = 0.6 \times 10^{-6}$. The cyan clear curves are the systematic effects at 1, 2, 3, $5f_{\rm HWP}$, as discussed in section 4.3.2. Since the signal is quasi-periodic, with period $T_{\rm payload}$, its Fourier transform peaks at the modulation frequency $4f_{\rm HWP}$ and then in frequency shifts equal to $\Delta f = 1/T_{\rm payload}$, clearly visible in the bottom figure.

the timeline; temperature data are centered around 0 frequency, and polarization data around $4f_{\rm HWP}$. The magenta line is is the noise for a single detector. Vertical dashed lines represent harmonics of the HWP spin frequency. The polarization signal is well contained within the $[3f_{\rm HWP}; 5f_{\rm HWP}]$ range. Figure 19 presents the results of this analysis in terms of B-modes angular power spectrum. The black lines are the B-modes angular power spectra in case of $r = 0$ and $r = 0.01$, which is the limit of our sensitivity. The coloured lines represent the residual power spectra of the case with systematic effects and notch filter, versus the ideal case, without systematic effects nor filters. Notably, in this figure we consider a combination of several systematic effects: instrumental polarization, HWP angle errors, HWP angle offset, uncertainty in the measurement of the HWP angular velocity. Applying

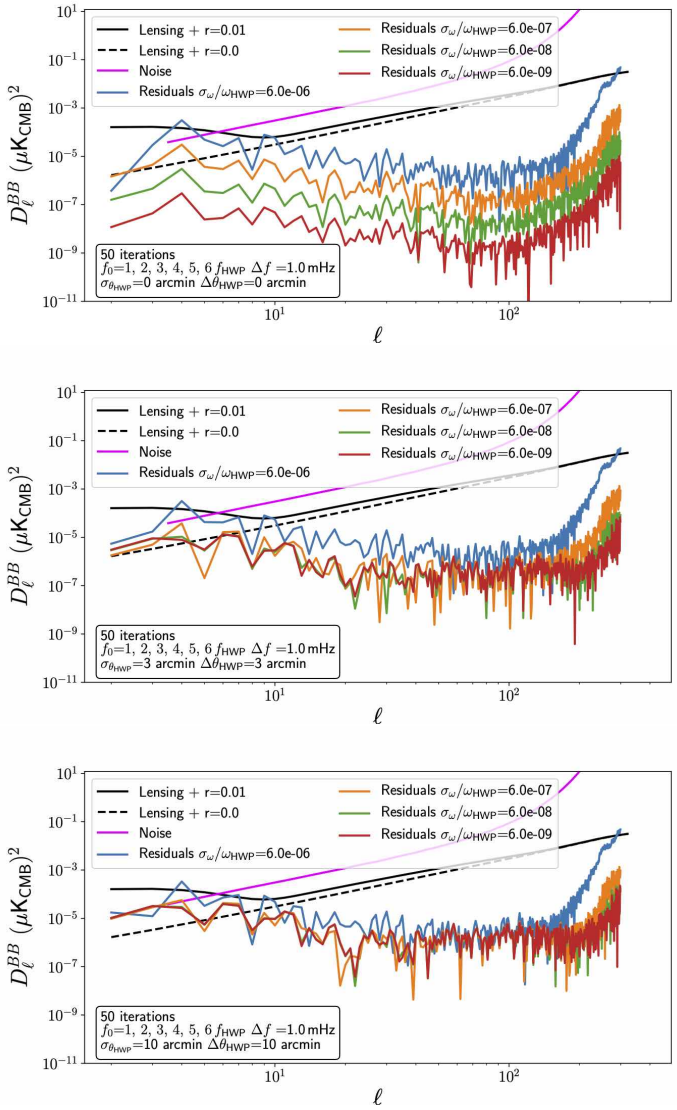

Figure 19. Impact of HWP synchronous systematic effects at $1f_{\rm HWP}$, $2f_{\rm HWP}$, $3f_{\rm HWP}$, $4f_{\rm HWP}$ and $5f_{\rm HWP}$, with amplitude 10 mK, 10 mK, 1 mK, 1 mK, and 1 mK respectively. Black lines: B-modes angular power spectra for $r = 0$ (dashed) and $r = 0.01$ (continuous). Coloured lines: residual of B-modes power spectrum of simulated map with HWP synchronous systematic effects and notch filters, with respect to simulated map without systematic effects nor filters. The three panels are for the cases: (*top*) with HWP synchronous systematic effects, and HWP instability; (*mid*) with HWP synchronous systematic effects, HWP instability, $\Delta\theta_{\rm HWP} = 3'$ and $\sigma_{\theta_{\rm HWP}} = 3'$; (*bottom*) with HWP synchronous systematic effects, HWP instability, $\Delta\theta_{\rm HWP} = 10'$ and $\sigma_{\theta_{\rm HWP}} = 10'$; in all panels, there are 4 continuous lines, for different angular speed uncertainty: $\sigma_{\omega_{\rm HWP}}/\omega_{\rm HWP} = [0.6\times10^{-8}, 0.6\times10^{-7}, 0.6\times10^{-6}, 0.6\times10^{-5}]$. The magenta line is the noise power spectrum after component separation.

r estimation pipeline (see section 5.2) to the maps contaminated by the combinations of systematic effects just described, we obtain a bias in r as reported in figure 20. The maps used to produce values in this figure are simulated with $\sigma_{\theta_{\rm HWP}} = 10'$; $\Delta\theta_{\rm HWP} = 10'$; synchronous systematic effects at [1,2,3,4,5] $f_{\rm HWP}$ with amplitude [10,10,1,1,1] mK respectively; and $\sigma_\omega/\omega_{\rm HWP}$ as in the abscissas.

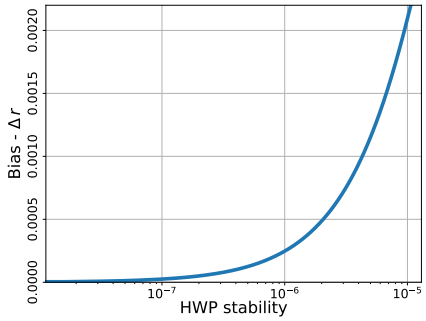

Figure 20. Bias in r due to instability of the HWP, combined with instrumental polarization, HWP angle offset, and HWP angle measurement error.

Parameter	Requirement
Instrumental polarization	$< 0.04\%$
Cross polarization	$< 2\%$
Polarization angle recovery	$< 40'$
WG angle error	$\Delta\phi_{\rm WG} < 20'$
HWP angle offset	$\Delta\theta_{\rm HWP} < 10'$
HWP angle noise	$\sigma_{\theta_{\rm HWP}} < 10'$
Time constant knowledge	$\sigma_{\tau_{\rm LP}} < 1.0\,{\rm ms}$
HWP angular velocity knowledge	$\sigma_{\omega_{\rm HWP}}/\omega_{\rm HWP} < 5 \times 10^{-6}$

Table 8. LSPE-SWIPE main systematic effects requirements. These requirements are derived considered the various effects jointly.

From this analysis, we set the requirements reported in table 8, for the most critical systematic effects for LSPE-SWIPE polarization measurement, considered jointly. The impact of the residual systematic effects will be assesses by estimation of the bias into angular power spectra by means of end-to-end Monte Carlo simulations.

4.4 LSPE-SWIPE calibration

As in the case of Strip, the SWIPE calibration will be performed in multiple stages:

1. at sub-system level: components will be tested individually in order to define specific properties. These components include optical filters, HWP, horns, detectors, readout electronics;

2. at system level: the integrated system, will undergo a long list of calibration tests. These include test of the polarization properties of the integrated system as a function of frequency, band-integrated polarization properties, angle dependent polarization properties, band-pass definition, angular response (by means of a far field thermal source). It is worth noting that the properties of the instrument are not expected to change from ground to the stratosphere, given that the thermal configuration is the same; the major change will be in the different background which is expected to modify the detector responsivity, to be confirmed in flight;

3. during observation: during observation the payload will undergo a limited number of tests for the verification. In particular these tests will be devoted to update of detector responsivity,

update of the pointing direction of each detector with respect to the telescope reference frame, and confirmation of the polarization properties of the system, by observation of the Crab nebula [89], and by minimization of the E-B modes correlation.

5 Results

In this section we present the component separation and the likelihood methods, and we deliver the main results of LSPE in terms of cosmological parameters. It is assumed that the systematic effects are within the requirement defined in section 4.

5.1 Component separation

Component separation is a key element in CMB data analysis, and it turns out to be particularly challenging for the extraction of CMB polarization (see e.g. [90]). In particular, diffuse Galactic dust and synchrotron emissions are the most relevant foregrounds in polarization. For the analysis presented in this paper, we consider the component separation apparatus represented by the `ForeGroundBuster`[11], which is currently used to assess the foreground cleaning capabilities of a number of CMB B-mode probes [91, 92]. The method fits, in each pixel observed by both Strip and SWIPE, for CMB signal, amplitude, spectral indices and curvature of synchrotron, temperature, amplitude and emissivity of dust. In our analysis, we include thermal dust and synchrotron as polarized foregrounds. The synchrotron spectral brightness is modeled as a power law decaying in frequency with a constant spectral index $\beta_s = -3$: $I_s(\nu, \hat{n}) = A_s(\hat{n})(\nu/\nu_0)^{\beta_s}$, where $A_s(\hat{n})$ is the synchrotron amplitude. The dust component is modeled as a grey body, i.e. an almost thermal component at a temperature of $T_d = 20\,\mathrm{K}$, heated back by starlight, represented by a frequency dependent optical depth, with spectral index $\beta_d = 1.54$: $I_d(\nu, \hat{n}) = \tau_0(\hat{n})(\nu/\nu_0)^{\beta_d} B(\nu, T_d)$. The component separation procedure is performed only on polarization maps and it recovers the value of the spectral indices β_s, β_d (a single value for the full map), as well as the amplitude of the synchrotron signal $A_s(\hat{n})$ and dust optical depth $\tau_0(\hat{n})$ in each direction. Together with the LSPE bands, we also consider the observations of the *Planck* satellite between 30 and 353 GHz [93], and the ones of QUIJOTE at 11 GHz [16, 94]. All maps, including noise realizations, use the `HEALPix`[12] at $N_{\mathrm{side}} = 128$. In the component separation runs for this paper, in order to deal with frequency channels at different resolutions, we smoothed all the component maps to a Gaussian beam with 85 arcmin FWHM, which is the largest beam associated to LSPE channels.

A key element of component separation is the W matrix, which is the linear operator that mixes the frequency maps in the component maps, taking into account the sensitivity and the contribution of each frequency to each astrophysical component. The elements $W_{i,j}$ of the W matrix (often referred as *weights*) admit negative values for frequencies that must be subtracted in order to solve for the astrophysical component. Frequency bands and weights for each component are shown in table 9.

From this table it is clear that the 145 GHz channel is the most important one for reconstructing the CMB, clearly adding sensitivity to the currently available datasets. The table also quantitatively shows relevance for what concerns the wings of the frequency interval for fitting and subtracting foregrounds. In table 10, we show minimal setup of our baseline, where we have used just the 30 GHz channel of *Planck* and LSPE frequencies. Moreover in table 11 we show the accuracy of the component separation in terms of dust and synchrotron spectral indices. As an illustration, figure 21 shows the polarization CMB power spectra obtained averaging 1000 simulations after component

[11] https://github.com/fgbuster/fgbuster

[12] Hierarchical Equal Latitude Pixelization

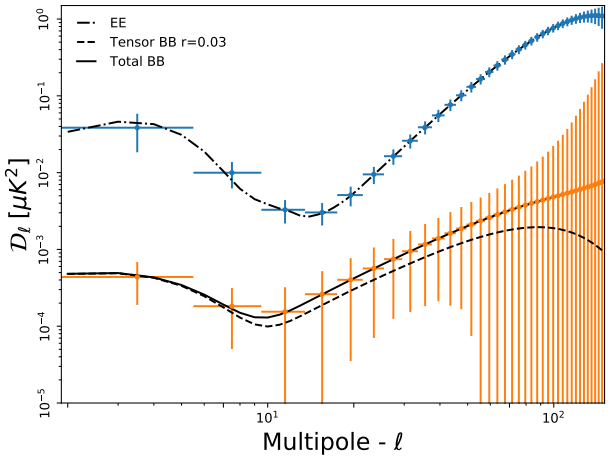

Figure 21. CMB E-modes (blue) and B-modes (orange) power spectra averaged over 1000 simulations after Component separation.

Band (GHz)	Probes	w_{CMB} $\times 10^3$	w_{Dust} $\times 10^3$	w_{Synch} $\times 10^3$
11	Q	−1.1	0.24	56
30	P	2.52	−1.1	18
43	ST	4.43	−1.9	8.03
44	P	1.92	−0.82	3.2
70	P	2.85	−1.1	0.86
100	P	14	−5.3	0.41
143	P	26.4	−7.4	−2.2
145	SW	1226	−330	−107
210	SW	−130	204	5.6
217	P	−7.1	8.5	0.48
240	SW	−150	130	14
353	P	−9.9	6.5	1.2

Table 9. Component separation weights for each component in each channel, in the Probes column P, Q, ST and SW stand for: *Planck*, QUIJOTE, Strip and SWIPE respectively.

separation. As byproduct of the component separation procedure LSPE will also provide precious information about synchrotron and thermal dust emissions in our Galaxy. This will be valuable to map the galactic magnetic field and to study the properties of the ionized gas and of the diffuse interstellar dust in the Milky Way.

5.2 Likelihood

The likelihood used in the parameter estimation is based on maps of Stokes parameters T, Q, U in `HEALPix` format. For the temperature map we assume perfect component separation outside a Galactic masks with 2 μK per pixel of white noise[13]. The polarization maps after the component separation procedure, described in the previous section, are modelled as a sum of CMB signal, instrumental Gaussian noise and foreground Gaussian residuals. In this scenario the full likelihood expression

[13]In temperature we substantially assume signal dominated observations. The white noise added is only necessary for regularizing the inversion of the temperature block of the TQU covariance matrix, see e.g. [95]

Band (GHz)	Probes	w_{CMB} $\times 10^3$	w_{Dust} $\times 10^3$	w_{Synch} $\times 10^3$
30	P	−15	2.7	870
43	ST	−2.6	−0.45	390
145	SW	1400	−410	−1600
210	SW	−190	240	28
240	SW	−202	160	340

Table 10. Component separation weights for each component in each channel for the minimal case: *Planck* + LSPE (Strip & SWIPE).

Parameter	Mean	σ
β_d	1.539	0.001
β_s	−2.999	0.002

Table 11. Dust and synchrotron spectral indices obtained by parametric component separation. The component separation algorithm fits for a single value in each map. The uncertainties are derived from the standard deviation of 1000 realizations of the noise in the maps.

reads

$$\mathcal{P}(\vec{m}|C_\ell) = \frac{1}{2\pi|\mathsf{C}(C_\ell)|^{1/2}} \exp\left(-\frac{1}{2}\vec{m}^{\mathsf{T}}\,[\mathsf{C}(C_\ell)]^{-1}\,\vec{m}\right), \tag{5.1}$$

where $\vec{m} \equiv T, Q, U$ is the data vector and C is total covariance matrix defined as the sum of signal and noise parts as

$$\mathsf{C}(C_\ell) = \sum_{\ell=2}^{\ell_{\rm max}} \sum_{XY} \frac{2\ell+1}{4\pi} B_\ell^2 C_\ell^{XY} \mathsf{P}_\ell^{XY} + \mathsf{N}, \tag{5.2}$$

here B_ℓ is the beam window function, P_ℓ^{XY} are the associated Legendre polynomials, as defined in [96], and N is the pixel-pixel noise covariance matrix.

In order to speed up the computation we perform the likelihood evaluation on lower resolution maps, still able to keep the full potentiality of LSPE maps. We consider two resolutions, `HEALPix` $N_{\rm side} = 16$, with a Gaussian beam of FWHM $= 440'$, which allows to explore comfortably the reionization peak of E-modes, and `HEALPix` $N_{\rm side} = 64$, with a Gaussian beam of FWHM $= 110'$, capable to measure both reionization and recombination peak of B-modes.

The likelihood analysis is performed simultaneously on a Monte Carlo of 1000 CMB, noise and residual foreground realizations. For each realization we estimate the reionization optical depth τ and the tensor-to-scalar ratio r. For each instrumental configuration the LSPE uncertainty on τ and r is computed taking the average over the 1000 realizations of the $\log\left(\mathcal{P}(\vec{m}|C_\ell)\right)$. In this way we efficiently take care of the scatter due to cosmic variance and instrumental noise. The other ΛCDM parameters are not sampled in this analysis, nonetheless we verified that opening the parameter exploration to full ΛCDM, and including a high-ℓ likelihood with noise performance compatible with *Planck*, provides equivalent results.

5.3 Reionization optical depth constraints

Measuring the polarization at very large scales, in particular the so-called reionization bump, allows to constrain directly the Thompson scattering optical depth τ. LSPE provides a cosmic variance limited measure of the polarization signal at very large scales ($\ell \lesssim 10$) on $\sim 35\%$ of the sky. For the analysis presented here we conservatively consider a smaller portion, $f_{\rm sky} \simeq 25\%$, removing regions

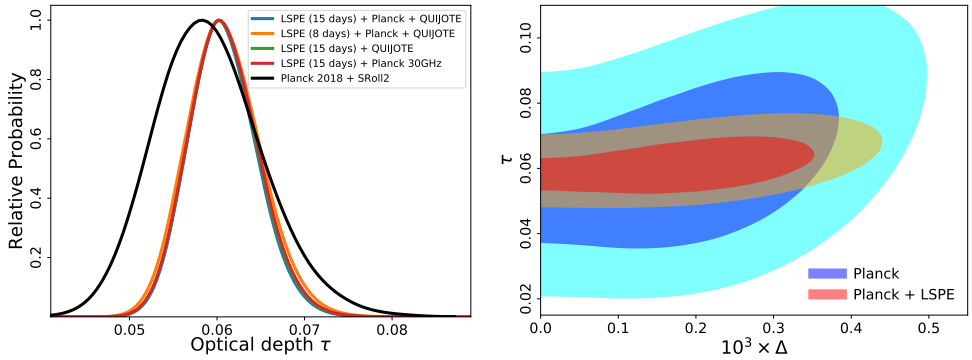

Figure 22. *Left*: posterior probability for optical depth τ. The colored lines show different component separation configurations, see text for details. The black line shows the current best estimate on τ. *Right*: Joint posterior probability for scale parameter Δ in (Mpc^{-1}) and optical depth τ. Blue and cyan are 68% and 95% CL for *Planck*; red and orange for *Planck* and LSPE.

Data Combination	σ_τ
Strip + SWIPE 15 + QUIJOTE + *Planck*	0.0037
Strip + SWIPE 8 + QUIJOTE + *Planck*	0.0040
Strip + SWIPE 15 + QUIJOTE	0.0038
Strip + SWIPE 15 + *Planck* 30GHz	0.0038

Table 12. Forecasted $1-\sigma$ errors on τ for different data combination obtained marginalizing over $\ln(10^{10}A_s)$. SWIPE 15 and SWIPE 8 stand respectively for 15 and 8 days of mission time, in both cases the effective time used for the sky survey is reduced by 1 day used for calibration and ancillary operations.

close to the Galactic plane potentially contaminated by residual foregrounds. The LSPE sensitivity on such sky fraction overcomes the current best estimates provided by *Planck* HFI, i.e. $\tau = 0.059 \pm 0.006$ [97], reaching $1-\sigma$ error on τ of ~ 0.004.

The constraints on the reionization optical depth τ are reported in table 12 and figure 22 for different data combinations. For Strip we consider 2 years of observations, for SWIPE we explore two possibilities, 15 days (SWIPE 15) or 8 days of observation (SWIPE 8). *Planck* and QUIJOTE are assumed with their nominal observational strategies and only considered in the portion of sky in common with LSPE. The τ constraints are rather stable showing that even after 8 days of SWIPE observations we reach the mission goal. Furthermore, even in a minimal configuration which considers only LSPE plus *Planck* 30 GHz as additional synchrotron tracer, the τ measure does not change substantially, showing that we are not heavily dependent on the usage of external datasets.

LSPE can also provide valuable information on the study of one of the most discussed anomalies related to CMB, i.e. the lack of power at large angular scales in the anisotropy power spectrum [98–102]. Entering in details about modelling and possible constraining techniques is beyond the scope of this paper. Here we only want to show how, in the context of a specific model such as the one predicting early departure from slow-roll inflation [see e.g. 103, 104], LSPE provides valuable constraints, being able to break completely the remaining degeneracy that such models still have with the reionization optical depth τ in the current CMB data [105, 106]. As an example, the model

Data Combination	σ_r	95%cl
Strip + SWIPE 15 + QUIJOTE + *Planck*	0.0093	0.015
Strip + SWIPE 8 + QUIJOTE + *Planck*	0.013	0.024
Strip + SWIPE 15 + QUIJOTE	0.0098	0.016
Strip + SWIPE 15 + *Planck* 30GHz	0.010	0.018

Table 13. Forecasted sensitivity on the tensor-to-scalar ratio r. The second column shows $1-\sigma$ errors assuming an input $r = 0.03$. The third column shows 95% c.l. upper limits assuming no tensor B-modes (i.e. $r = 0$).

described in [107] modifies the primordial scalar power spectrum according to:

$$P_\Delta(k) = A_s \frac{(k/k_*)^3}{\left[(k/k_*)^2 + (\Delta/k_*)^2\right]^{2-\frac{n_s}{2}}},$$

where k is the primordial perturbation wavenumber in Mpc^{-1}, A_s and n_s are respectively the amplitude and the tilt of scalar perturbations, $k_* = 0.05\,\mathrm{Mpc}^{-1}$ is the pivot scale, and Δ is a characteristic scale[14] which breaks the power-law at very low wavenumbers damping both temperature and polarization power spectra at low multipoles. In this particular case, as shown in right panel of figure 22, LSPE improves the *Planck* constraint, substantially cancelling the degeneration with τ.

5.4 Tensor-to-scalar ratio constraints

The angular resolution of LSPE and the observational strategy allow to measure simultaneously both the reionization and the recombination peak of the primordial B-modes. This makes LSPE an extremely complete and unique instrument observing a region of the sky not entirely visible from the southern hemisphere. Nevertheless the relatively small sky fraction usable, if compared with a satellite mission, limits our sensitivity at very large scales. The aggregate sensitivity allows to detect $r = 0.03$ with $3-\sigma$ significance for different data combinations. In this case limiting the mission time of SWIPE to 8 days induces a non-negligible effect, reducing the r significance down to $\sim 2.3\,\sigma$, still within the mission requirements. In case of no primordial B-modes the equivalent $1-\sigma$ error on r is $\sigma_r = 0.007$ when we combine Strip and SWIPE with both *Planck* and QUIJOTE as foreground tracers. In table 13 we report the constraints on r for the different data combination analyzed, in this case two input r values have been considered, i.e., $r = 0.03$ and $r = 0$.

5.5 Constraints on cosmic birefringence

CMB polarization data can also be used to probe cosmic birefringence (CB), i.e., the in vacuum rotation of the plane of linear polarization during propagation [108]. In this section we focus on isotropic birefringence rotation, see e.g., [109–114]. For those measurements the calibration of the polarization angle of polarimeters is a key aspect, since miscalibration of such angle is completely degenerate with the rotation induced by CB, see section 4.3.1 and references therein[15]. Assuming negligible calibration error on the polarization angle, we can constrain CB angle, α_{CB}, with same technique used to constrain τ and r, i.e. a pixel based approach for the likelihood estimation. Another possible approach is to use the so called D-Estimators, as defined in e.g. [113], which employ TB and

[14] For the forecast presented in this paper we choose $\Delta = 0.0002\,\mathrm{Mpc}^{-1}$ as fiducial value.

[15] A new method has been proposed recently which aims at breaking the degeneracy between birefringence angle and instrumental polarization angle [115, 116].

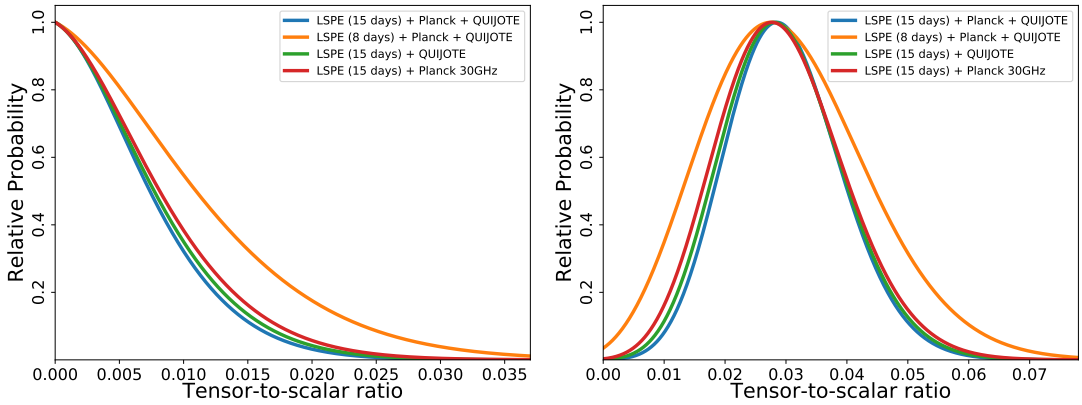

Figure 23. Posterior probability for tensor to scalar ratio r in case of $r = 0$ (*left*) and $r = 0.03$ (*right*). The colored lines show different component separation configurations, see text for details.

Data Combination	$\sigma^{\rm PB}_{\alpha_{\rm CB}}$	$\sigma^{\rm DE}_{\alpha_{\rm CB}}$
Strip + SWIPE 15 + QUIJOTE + *Planck*	0.22	0.19
Strip + SWIPE 8 + QUIJOTE + *Planck*	0.30	0.29
Strip + SWIPE 15 + QUIJOTE	0.23	0.21
Strip + SWIPE 15 + *Planck* 30 GHz	0.24	0.22

Table 14. Forecasted sensitivity on the cosmic birefringence angle $\alpha_{\rm CB}$ in degree. The second and third columns show $1-\sigma$ errors obtained with the pixel based approach and D-Estimators approach, respectively.

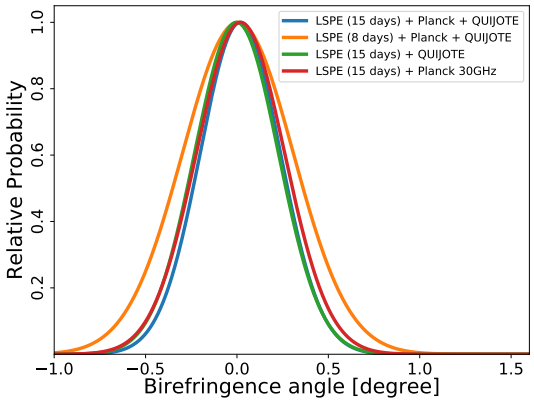

Figure 24. Posterior probability for cosmic birefringence angle obtained with the pixel based likelihood.

EB power spectra. In table 14 we report constraints of $\alpha_{\rm CB}$ for different data combination for both the approaches mentioned above, in figure 24 we show the posteriors obtained with the pixel based method. LSPE data will allow to constrain uniform birefringence angle down to 0.2°, improving by a factor 3 the current best estimate [114].

6 Conclusion

The Large Scale Polarization Explorer is a program dedicated to the measure of the CMB polarization and its B-mode component in particular. We have presented the instruments design, and a detailed

forecast of its performance. LSPE can put an upper limit to the tensor-to-scalar ratio at the level of 10^{-2} and detect a $r = 0.03$ with 95% confidence limits. Moreover, LSPE can improve constraints on other parameters, like the optical depth of the Universe to the CMB, τ, and the rotation angle originated by a cosmic birefringence. This analysis is obtained by a full set of end-to-end simulations, including detailed noise estimation, instrument observations, map-making, component separation, and cosmological parameters extraction. We also present techniques for the control and removal of Half-Wave plate synchronous systematic effects.

With its rotating HWP, LSPE-SWIPE represents an important pathfinder of the forthcoming LiteBIRD mission [117] from the point of view of the instrument requirements, instrument design, calibration, control of systematic effects, and data analysis.

Acknowledgments

The development of LSPE is supported by ASI (grant LSPE I/022/11/0) and INFN. We acknowledge the usage of the `HEALPix`[118] and am software packages, computational resources from NERSC, Cineca and CNAF. We acknowledge support from the COSMOS network (www.cosmosnet.it) through the ASI (Italian Space Agency) Grants 2016-24-H.0 and 2016-24-H.1-2018, and Sapienza University. JARM, RGS and MPdT acknowledge financial support from the Spanish Ministry of Science and Innovation (MICINN) under the project AYA2017-84185-P, and the European Union's Horizon 2020 research and innovation programme under grant agreement number 687312 (RADIOFOREGROUNDS).

References

[1] U. Seljak and M. Zaldarriaga, *Signature of gravity waves in the polarization of the microwave background*, *Phys. Rev. Lett.* **78** (1997) 2054.

[2] M. Kamionkowski and E. D. Kovetz, *The Quest for B Modes from Inflationary Gravitational Waves*, *Annu. Rev. Astron. Astr.* **54** (2016) 227.

[3] P. A. R. Ade, Z. Ahmed, R. W. Aikin, K. D. Alexander, D. Barkats, S. J. Benton et al., *Constraints on Primordial Gravitational Waves Using Planck, WMAP, and New BICEP2/Keck Observations through the 2015 Season*, *Phys. Rev. Lett.* **121** (2018) 221301 [1810.05216].

[4] P. de Bernardis, S. Aiola, G. Amico, E. Battistelli, A. Coppolecchia, A. Cruciani et al., *SWIPE: a bolometric polarimeter for the Large-Scale Polarization Explorer*, in *Millimeter, Submillimeter, and Far-Infrared Detectors and Instrumentation for Astronomy VI*, vol. 8452 of *Proc. SPIE*, p. 84523F, Sept., 2012, DOI [1208.0282].

[5] S. Aiola, G. Amico, P. Battaglia, E. Battistelli, A. Baó, P. de Bernardis et al., *The Large-Scale Polarization Explorer (LSPE)*, in *Ground-based and Airborne Instrumentation for Astronomy IV*, vol. 8446 of *Proc. SPIE*, p. 84467A, Sept., 2012, DOI.

[6] M. Bersanelli, A. Mennella, G. Morgante, M. Zannoni, G. Addamo, A. Baschirotto et al., *A coherent polarimeter array for the Large Scale Polarization Explorer (LSPE) balloon experiment*, in *Ground-based and Airborne Instrumentation for Astronomy IV*, vol. 8446 of *Proc. SPIE*, p. 84467C, Sept., 2012, DOI [1208.0164].

[7] L. Lamagna, G. Addamo, P. A. R. Ade, C. Baccigalupi, A. M. Baldini, P. M. Battaglia et al., *Progress report on the Large Scale Polarization Explorer*, *J. Low Temp. Phys.* (2020) arXiv:2005.01187 [2005.01187].

[8] F. Incardona, *Observing the polarized Cosmic Microwave Background from the Earth : scanning strategy and polarimeters test for the LSPE / STRIP instrument*, Ph.D. thesis, University of Milan, 2020.

[9] N. Krachmalnicoff, E. Carretti, C. Baccigalupi, G. Bernardi, S. Brown, B. M. Gaensler et al., *S-PASS view of polarized Galactic synchrotron at 2.3 GHz as a contaminant to CMB observations*, *Astron. Astrophys.* **618** (2018) A166 [1802.01145].

[10] J. A. Castro-Almazán, C. Muñoz-Tuñón, B. García-Lorenzo, G. Pérez-Jordán, A. M. Varela and I. Romero, *Precipitable Water Vapour at the Canarian Observatories (Teide and Roque de los Muchachos) from routine GPS*, in *Observatory Operations: Strategies, Processes, and Systems VI*, vol. 9910 of *Society of Photo-Optical Instrumentation Engineers (SPIE) Conference Series*, p. 99100P, Jul, 2016, DOI.

[11] C. M. Gutiérrez, R. Rebolo, R. A. Watson, R. D. Davies, A. W. Jones and A. N. Lasenby, *The Tenerife Cosmic Microwave Background Maps: Observations and First Analysis*, *Astrophys. J.* **529** (2000) 47 [astro-ph/9903196].

[12] B. Femenía, R. Rebolo, C. M. Gutiérrez, M. Limon and L. Piccirillo, *The Instituto de Astrofísica de Canarias-Bartol Cosmic Microwave Background Anisotropy Experiment: Results of the 1994 Campaign*, *Astrophys. J.* **498** (1998) 117 [astro-ph/9711225].

[13] D. L. Harrison, J. A. Rubiño-Martin, S. J. Melhuish, R. A. Watson, R. D. Davies, R. Rebolo et al., *A measurement at the first acoustic peak of the cosmic microwave background with the 33-GHz interferometer*, *Mon. Not. Roy. Astron. Soc.* **316** (2000) L24 [astro-ph/0004357].

[14] S. Fernández-Cerezo, C. M. Gutiérrez, R. Rebolo, R. A. Watson, R. J. Hoyland, S. R. Hildebrandt et al., *Observations of the cosmic microwave background and galactic foregrounds at 12-17GHz with the COSMOSOMAS experiment*, *Mon. Not. Roy. Astron. Soc.* **370** (2006) 15 [astro-ph/0601203].

[15] R. A. Watson, P. Carreira, K. Cleary, R. D. Davies, R. J. Davis, C. Dickinson et al., *First results from the Very Small Array - I. Observational methods*, *Mon. Not. Roy. Astron. Soc.* **341** (2003) 1057 [astro-ph/0205378].

[16] J. A. Rubiño-Martín, R. Rebolo, M. Aguiar, R. Génova-Santos, F. Gómez-Reñasco, J. M. Herreros et al., *The QUIJOTE-CMB experiment: studying the polarisation of the galactic and cosmological microwave emissions*, in *Ground-based and Airborne Telescopes IV*, vol. 8444 of *Society of Photo-Optical Instrumentation Engineers (SPIE) Conference Series*, p. 84442Y, Sep, 2012, DOI.

[17] S. Oguri, J. Choi, T. Damayanthi, M. Hattori, M. Hazumi, H. Ishitsuka et al., *GroundBIRD: Observing Cosmic Microwave Polarization at Large Angular Scale with Kinetic Inductance Detectors and High-Speed Rotating Telescope*, *J. Low Temp. Phys.* **184** (2016) 786.

[18] A. C. Taylor, *Clover - A B-mode polarization experiment*, *New Astron. Rev.* **50** (2006) 993 .

[19] C. Franceschet, S. Realini, A. Mennella, G. Addamo, A. Baú, P. M. Battaglia et al., *The STRIP instrument of the Large Scale Polarization Explorer: microwave eyes to map the Galactic polarized foregrounds*, in *Millimeter, Submillimeter, and Far-Infrared Detectors and Instrumentation for Astronomy IX*, vol. 10708 of *Society of Photo-Optical Instrumentation Engineers (SPIE) Conference Series*, p. 107081G, Jul, 2018, DOI.

[20] S. Realini, C. Franceschet and A. Mennella, *Modelling the radiation pattern of a dual circular polarization system*, *J. Instrum.* **14** (2019) P03005.

[21] O. A. Peverini, G. Virone, F. Del Torto, C. Franceschet, F. Villa, M. Lumia et al., *Q-band antenna-feed system for the Large Scale Polarization Explorer balloon experiment*, in *2015 International Conference on Electromagnetics in Advanced Applications (ICEAA)*, pp. 883–886, IEEE, sep, 2015, DOI.

[22] F. Del Torto, M. Bersanelli, F. Cavaliere, A. De Rosa, O. D'Arcangelo, C. Franceschet et al., *W-band prototype of platelet feed-horn array for CMB polarisation measurements*, *J. Instrum.* **6** (2011) 6009 [1107.1157].

[23] S. Y. Eom and Y. B. Korchemkin, *A New Comb Circular Polarizer Suitable for Millimeter-Band Application*, *ETRI Journal* **28** (2006) 656.

[24] G. Virone, O. A. Peverini, M. Lumia, G. Addamo and R. Tascone, *Platelet Orthomode Transducer for Q-Band Correlation Polarimeter Clusters*, *IEEE T. Microw. Theory* **62** (2014) 1487.

[25] QUIET Collaboration, D. Araujo, C. Bischoff, A. Brizius, I. Buder, Y. Chinone et al., *Second season QUIET observations: Measurements of the cosmic microwave background polarization power spectrum at 95 GHz*, *Astrophys. J.* **760** (2012) [1207.5034].

[26] Y.-L. Chen, T. Chiueh and H.-F. Teng, *A 77-118 GHz RESONANCE-FREE SEPTUM POLARIZER*, *Astrophys. J., Suppl. Ser.* **211** (2014) 11.

[27] QUIET Collaboration, C. Bischoff, A. Brizius, I. Buder, Y. Chinone, K. Cleary et al., *First Season QUIET Observations: Measurements of Cosmic Microwave Background Polarization Power Spectra at 43 GHz in the Multipole Range* $25 \leq \ell \leq 475$, *Astrophys. J.* **741** (2011) 111 [1012.3191].

[28] A. Iarocci, P. Benedetti, F. Caprara, A. Cardillo, F. di Felice, G. di Stefano et al., *PEGASO: An ultra light long duration stratospheric payload for polar regions flights*, *Adv. Space Res.* **42** (2008) 1633.

[29] S. Peterzen, S. Masi, P. Dragoy, R. Ibba and D. Spoto, *Long Duration Balloon flights development. (Italian Space Agency)*, *Mem. Soc. Astron. Italiana* **79** (2008) 792.

[30] S. Peterzen, P. Ubertini, S. Masi, R. Ibba, M. Ivano, A. Cardillo et al., *Space and Earth Observations from Stratospheric Balloons*, in *37th COSPAR Scientific Assembly*, vol. 37 of *COSPAR Meeting*, p. 2419, 2008.

[31] S. Peterzen, S. Masi and P. Debernardis, *Polar Stratospheric Research Platforms -Ballooning in the Polar Regions*, in *38th COSPAR Scientific Assembly*, vol. 38 of *COSPAR Meeting*, p. 4, 2010.

[32] P. de Bernardis, S. Masi and OLIMPO and LSPE Teams, *Precision CMB measurements with long-duration stratospheric balloons: activities in the Arctic*, in *Astrophysics from Antarctica*, M. G. Burton, X. Cui and N. F. H. Tothill, eds., vol. 288 of *IAU Symposium*, pp. 208–213, Jan., 2013, DOI.

[33] F. Piacentini, A. Coppolecchia, P. de Bernardis, G. Di Stefano, A. Iarocci, L. Lamagna et al., *Winter long duration stratospheric balloons from Polar regions*, *arXiv e-prints* (2018) arXiv:1810.05565 [1810.05565].

[34] P. de Bernardis, E. Aquilini, A. Boscaleri, M. de Petris, M. Gervasi, L. Martinis et al., *ARGO: a balloon-borne telescope for measurements of the millimeter diffuse sky emission*, *Astron. Astrophys.* **271** (1993) 683.

[35] B. P. Crill, P. A. R. Ade, D. R. Artusa, R. S. Bhatia, J. J. Bock, A. Boscaleri et al., *BOOMERANG: A Balloon-borne Millimeter-Wave Telescope and Total Power Receiver for Mapping Anisotropy in the Cosmic Microwave Background*, *Astrophys. J., Suppl. Ser.* **148** (2003) 527 [astro-ph/0206254].

[36] S. Masi, P. A. R. Ade, J. J. Bock, J. R. Bond, J. Borrill, A. Boscaleri et al., *Instrument, method, brightness, and polarization maps from the 2003 flight of BOOMERanG*, *Astron. Astrophys.* **458** (2006) 687 [astro-ph/0507509].

[37] A. Benoît, P. Ade, A. Amblard, R. Ansari, E. Aubourg, J. Bartlett et al., *Archeops: a high resolution, large sky coverage balloon experiment for mapping cosmic microwave background anisotropies*, *Astropart. Phys.* **17** (2002) 101 [astro-ph/0106152].

[38] S. Masi, M. Calvo, L. Conversi, P. de Bernardis, M. de Petris, G. de Troia et al., *A balloon-borne survey of the mm/sub-mm sky: OLIMPO*, in *17th ESA Symposium on European Rocket and Balloon Programmes and Related Research*, B. Warmbein, ed., vol. 590 of *ESA Special Publication*, pp. 581–586, Aug., 2005.

[39] A. Paiella, A. Coppolecchia, L. Lamagna, P. Ade, E. Battistelli, M. G. Castellano et al., *Kinetic inductance detectors for the OLIMPO experiment: design and pre-flight characterization*, *J. Cosmol. Astropart. P.* **2019** (2019) 039.

[40] S. Masi, P. de Bernardis, A. Paiella, F. Piacentini, L. Lamagna, A. Coppolecchia et al., *Kinetic Inductance Detectors for the OLIMPO experiment: in-flight operation and performance*, *J. Cosmol. Astropart. P.* **2019** (2019) 003 [1902.08993].

[41] A. Boscaleri, V. Venturi and R. Colzi, *Time-domain computer simulation program as first step of a full digital high-precision pointing system for platform in balloon-borne remote sensing*, in *Infrared Technology XVI*, I. J. Spiro, ed., vol. 1341, pp. 58 – 65, International Society for Optics and Photonics, SPIE, 1990, DOI.

[42] A. Boscaleri, *A time domain design technique for high precision full digital pointing system in balloon-borne remote infrared sensing*, in *Acquisition, Tracking, and Pointing IV*, S. Gowrinathan, ed., vol. 1304, International Society for Optics and Photonics, SPIE, 1990, DOI.

[43] A. Boscaleri, V. Venturi and D. Tirelli, *The ARGO experiment pointing system as an example for other single-axis platform pointing systems*, *Meas. Sci. Technol.* **5** (1994) 190.

[44] F. Nati, P. de Bernardis, A. Iacoangeli, S. Masi, A. Benoit and D. Yvon, *A fast star sensor for balloon payloads*, *Rev. Sci. Instrum.* **74** (2003) 4169.

[45] J. F. Macías-Pérez, G. Lagache, B. Maffei, K. Ganga, A. Bourrachot, P. Ade et al., *Archeops in-flight performance, data processing, and map making*, *Astron. Astrophys.* **467** (2007) 1313 [astro-ph/0603665].

[46] P. Palumbo, E. Aquilini, P. Cardoni, P. de Bernardis, A. De Ninno, L. Martinis et al., *Balloon-borne ^{3}He cryostat for millimetre bolometric photometry*, *Cryogenics* **34** (1994) 1001.

[47] S. Masi, P. Cardoni, P. de Bernardis, F. Piacentini, A. Raccanelli and F. Scaramuzzi, *A long duration cryostat suitable for balloon borne photometry*, *Cryogenics* **39** (1999) 217.

[48] J. P. Bernard, P. Ade, Y. André, J. Aumont, L. Bautista, N. Bray et al., *PILOT: a balloon-borne experiment to measure the polarized FIR emission of dust grains in the interstellar medium*, *Exp. Astron.* **42** (2016) 199.

[49] A. Coppolecchia, L. Lamagna, S. Masi, P. Ade, G. Amico, E. Battistelli et al., *The long duration cryogenic system of the olimpo balloon-borne experiment: design and in-flight performance*, *Cryogenics* (2020) 103129.

[50] G. Coppi, P. de Bernardis, A. J. May, S. Masi, M. McCulloch, S. J. Melhuish et al., *Developing a long duration ^{3}He fridge for the LSPE-SWIPE instrument*, vol. 9912 of *Society of Photo-Optical Instrumentation Engineers (SPIE) Conference Series*, p. 991265. SPIE, 2016. 10.1117/12.2232448.

[51] K. Zilic, A. Aboobaker, F. Aubin, C. Geach, S. Hanany, N. Jarosik et al., *A double vacuum window mechanism for space-borne applications*, *Rev. Sci. Instrum.* **88** (2017) .

[52] G. dall'Oglio, P. de Bernardis, S. Masi and F. Melchiorri, *Measurement of the 3K Cosmic Background Noise in the Far Infrared*, in *Early Evolution of the Universe and its Present Structure*, G. O. Abell and G. Chincarini, eds., vol. 104 of *IAU Symposium*, p. 135, Jan., 1983.

[53] J. F. Macías-Pérez, G. Lagache, B. Maffei, K. Ganga, A. Bourrachot, P. Ade et al., *Archeops in-flight performance, data processing, and map making*, *Astron. Astrophys.* **467** (2007) 1313 [astro-ph/0603665].

[54] G. D'Alessandro, A. Paiella, A. Coppolecchia, M. G. Castellano, I. Colantoni, P. de Bernardis et al., *Ultra high molecular weight polyethylene: Optical features at millimeter wavelengths*, *Infrared Phys. Technol.* **90** (2018) 59 [1803.05228].

[55] S. Legg, L. Lamagna, G. Coppi, P. de Bernardis, G. Giuliani, R. Gualtieri et al., *Development of the multi-mode horn-lens configuration for the LSPE-SWIPE B-mode experiment*, in *Millimeter, Submillimeter, and Far-Infrared Detectors and Instrumentation for Astronomy VIII*, vol. 9914 of *Proceeding SPIE*, p. 991414, July, 2016, DOI.

[56] F. Columbro, P. G. Madonia, L. Lamagna, E. S. Battistelli, A. Coppolecchia, P. de Bernardis et al., *Swipe multi-mode pixel assembly design and beam pattern measurements at cryogenic temperature*, *Journal of Low Temperature Physics* **199** (2020) 312.

[57] A. C. Ludwig, *The definition of cross polarization.*, *IEEE T. Antenn. Propag.* **21** (1973) 116.

[58] G. Pisano, C. Tucker, P. A. R. Ade, P. Moseley and M. W. Ng, *Metal mesh based metamaterials for millimetre wave and thz astronomy applications*, in *2015 8th UK, Europe, China Millimeter Waves and THz Technology Workshop (UCMMT)*, pp. 1–4, 2015, DOI.

[59] G. Pisano, M. Ng, V. Haynes and B. Maffei, *A broadband metal-mesh half-wave plate for millimetre wave linear polarisation rotation*, in *Progress In Electromagnetics Research M*, vol. 25, pp. 101–114, 2012, DOI.

[60] G. Pisano, P. Ade, C. Tucker and M. W. Ng, *Large bandwidth mesh half-wave plates for millimetre and thz wave astronomy*, in *2015 40th International Conference on Infrared, Millimeter, and Terahertz waves (IRMMW-THz)*, pp. 1–1, 2015.

[61] T. Matsumura, H. Kataza, S. Utsunomiya, R. Yamamoto, M. Hazumi and N. Katayama, *Design and performance of a prototype polarization modulator rotational system for use in space using a superconducting magnetic bearing*, *IEEE Trans. Appl. Supercond.* **26** (2016) 1.

[62] B. Johnson, F. Columbro, D. Araujo, M. Limon, B. Smiley, G. Jones et al., *A large-diameter hollow-shaft cryogenic motor based on a superconducting magnetic bearing for millimeter-wave polarimetry*, *Rev. Sci. Instrum.* **88** (2017) .

[63] F. Columbro, P. de Bernardis and S. Masi, *A clamp and release system for superconductive magnetic bearings*, *Rev. Sci. Instrum.* **89** (2018) .

[64] P. de Bernardis, F. Columbro, S. Masi, A. Paiella and G. Romeo, *A simple method to measure the temperature and levitation height of devices rotating at cryogenic temperatures*, *Rev. Sci. Instrum.* **91** (2020) 045118 [https://doi.org/10.1063/5.0005498].

[65] D. Vaccaro, B. Siri, A. M. Baldini, M. Biasotti, F. Cei, V. Ceriale et al., *Tuning the T_C of Titanium Thin Films for Transition-Edge Sensors by Annealing in Argon*, *J. Low Temp. Phys.* **193** (2018) 1122.

[66] D. Vaccaro, A. M. Baldini, F. Cei, L. Galli, M. Grassi, D. Nicolò et al., *"The FDM readout for the LSPE/SWIPE TES bolometers"*, in *Millimeter, Submillimeter, and Far-Infrared Detectors and Instrumentation for Astronomy IX*, J. Zmuidzinas and J.-R. Gao, eds., vol. 10708, pp. 732 – 742, International Society for Optics and Photonics, Proc. SPIE, 2018, DOI.

[67] D. Vaccaro, A. Baldini, F. Cei, L. Galli, M. Grassi, D. Nicolò et al., *A frequency domain multiplexing system to readout the TES bolometers on the LSPE/SWIPE experiment*, *Nucl. Instrum. Meth. A* **936** (2019) 169.

[68] F. Fontanelli, M. Biasotti, A. Bevilacqua and F. Siccardi, *The front-end electronics of the LSPE-SWIPE experiment*, in *Space Telescopes and Instrumentation 2016: Optical, Infrared, and Millimeter Wave*, H. A. MacEwen, G. G. Fazio, M. Lystrup, N. Batalha, N. Siegler and E. C. Tong, eds., vol. 9904, pp. 1633 – 1638, International Society for Optics and Photonics, Proc. SPIE, 2016, DOI.

[69] J. Bezanson, A. Edelman, S. Karpinski and V. B. Shah, *Julia: A fresh approach to numerical computing*, *SIAM review* **59** (2017) 65.

[70] C. Bischoff, A. Brizius, I. Buder, Y. Chinone, K. Cleary, R. N. Dumoulin et al., *THE Q/U IMAGING EXPERIMENT INSTRUMENT*, *Astrophys. J.* **768** (2013) 9.

[71] K. Cleary, *Coherent polarimeter modules for the QUIET experiment*, in *Society of Photo-Optical Instrumentation Engineers (SPIE) Conference Series*, vol. 7741 of *Society of Photo-Optical Instrumentation Engineers (SPIE) Conference Series*, jul, 2010, DOI.

[72] S. Paine, *The am atmospheric model*, Sept., 2019. 10.5281/zenodo.3406496.

[73] M. N. Afsar, K. A. Korolev, L. Subramanian and I. I. Tkachov, *Complex Dielectric Measurements of Materials at Q- Band, V- Band and W- Band Frequencies with High Power Sources*, in *2005 IEEE Instrumentationand Measurement Technology Conference Proceedings*, vol. 1, pp. 82–87, 2005.

[74] J. W. Lamb, *Miscellaneous data on materials for millimetre and submillimetre optics*, *J. Infrared. Millim. W.* **17** (1996) 1997.

[75] J. M. Lamarre, *Photon noise in photometric instruments at far-infrared and submillimeter wavelengths*, *Appl. Opt.* **25** (1986) 870.

[76] R. Gualtieri, E. S. Battistelli, A. Cruciani, P. de Bernardis, M. Biasotti, D. Corsini et al., *Multi-mode TES Bolometer Optimization for the LSPE-SWIPE Instrument*, *J. Low Temp. Phys.* **184** (2016) 527 [1602.07744].

[77] A. Tartari, A. M. Baldini, F. Cei, L. Galli, M. Grassi, D. Nicolò et al., *Development and testing of the fdm read-out of the tes arrays aboard the lspe/swipe balloon-borne experiment*, *J. Low Temp. Phys.* **199** (2020) 212.

[78] M. Dobbs et al., *Frequency Multiplexed SQUID Readout of Large Bolometer Arrays for Cosmic Microwave Background Measurements*, *Rev. Sci. Instrum.* **83** (2012) 073113 [1112.4215].

[79] F. Incardona, M. Benetti, M. Bersanelli, C. Franceschet, D. Maino, A. Mennella et al., *Preliminary scanning strategy analysis for the LSPE-STRIP instrument*, in *Society of Photo-Optical Instrumentation Engineers (SPIE) Conference Series*, vol. 10708, p. 107082F, Jul, 2018, DOI.

[80] Planck Collaboration, P. A. R. Ade, J. Aumont, C. Baccigalupi, A. J. Banday, R. B. Barreiro et al., *Planck 2015 results. III. LFI systematic uncertainties*, *Astron. Astrophys.* **594** (2016) A3.

[81] Planck Collaboration, P. A. R. Ade, N. Aghanim, M. Ashdown, J. Aumont, C. Baccigalupi et al., *Planck 2015 results. IV. Low Frequency Instrument beams and window functions*, *Astron. Astrophys.* **594** (2016) A4.

[82] Planck Collaboration III, *Planck 2015 results. III. LFI systematic uncertainties*, *Astron. Astrophys.* **594** (2016) A3 [1507.08853].

[83] N. Krachmalnicoff, *Challenges for Present and Future Cosmic Microwave Background Observations: Systematic Effects and Foreground Emission in Polarization*, Ph.D. thesis, University of Milan, 2015.

[84] G. Montresor, *A responsivity calibration strategy for the LSPE-STRIP balloon experiment*, Master's thesis, University of Milan, 2012.

[85] F. Paonessa, L. Ciorba, G. Virone, P. Bolli, J. Monari, F. Perini et al., *Characterization of the Murchison Widefield Array Dipole with a UAV-mounted Test Source*, in *13th European Conference on Antennas and Propagation, EuCAP 2019*, pp. 1–4, European Association on Antennas and Propagation, 2019.

[86] G. Pisano, G. Savini, P. A. R. Ade, V. Haynes and W. K. Gear, *Achromatic half-wave plate for submillimeter instruments in cosmic microwave background astronomy: experimental characterization*, *Appl. Opt.* **45** (2006) 6982.

[87] L. Pagano, P. de Bernardis, G. de Troia, G. Gubitosi, S. Masi, A. Melchiorri et al., *CMB polarization systematics, cosmological birefringence, and the gravitational waves background*, *Phys. Rev. D* **80** (2009) 043522 [0905.1651].

[88] F. Columbro, E. S. Battistelli, A. Coppolecchia, G. D'Alessandro, P. de Bernardis, L. Lamagna et al., *The short wavelength instrument for the polarization explorer balloon-borne experiment: Polarization modulation issues*, *Astron. Nachr.* **340** (2019) 83 [1904.01891].

[89] J. Aumont, J. F. Macías-Pérez, A. Ritacco, N. Ponthieu and A. Mangilli, *Absolute calibration of the polarisation angle for future CMB B-mode experiments from current and future measurements of the Crab nebula*, *A&A* **634** (2020) A100 [1911.03164].

[90] A. Buzzelli, M. Migliaccio, G. de Gasperis, P. de Bernardis, S. Masi and N. Vittorio, *Impact of polarized foregrounds on LSPE-SWIPE observations*, in *J. Phys. Conf. Ser.*, vol. 956, p. 012002, Jan., 2018, DOI.

[91] P. Campeti, D. Poletti and C. Baccigalupi, *Principal component analysis of the primordial tensor power spectrum*, *J. Cosmol. Astropart. P.* **1909** (2019) 055 [1905.08200].

[92] R. Stompor, J. Errard and D. Poletti, *Forecasting performance of CMB experiments in the presence of complex foreground contaminations*, *Phys. Rev.* **D94** (2016) 083526 [1609.03807].

[93] Planck Collaboration I, *Planck 2018 results. I. Overview, and the cosmological legacy of Planck*, *Astron. Astrophys., in press* (2019) [1807.06205].

[94] J. A. Rubiño-Martín, Planck Collaboration and QUIJOTE Collaboration, *Cosmology with the Cosmic Microwave Background: Latest Results from the PLANCK satellite and the QUIJOTE experiment*, in *Highlights on Spanish Astrophysics X*, B. Montesinos, A. Asensio Ramos, F. Buitrago, R. Schödel, E. Villaver, S. Pérez-Hoyos et al., eds., pp. 32–43, Mar., 2019.

[95] Planck Collaboration V, *Planck 2018 results. V. Power spectra and likelihoods*, *Astron. Astrophys., submitted* (2019) [1907.12875].

[96] M. Tegmark and A. de Oliveira-Costa, *How to measure CMB polarization power spectra without losing information*, *Phys. Rev.* **D64** (2001) 063001 [astro-ph/0012120].

[97] L. Pagano, J.-M. Delouis, S. Mottet, J.-L. Puget and L. Vibert, *Reionization optical depth determination from Planck HFI data with ten percent accuracy*, *Astron. Astrophys.* **635** (2020) A99 [1908.09856].

[98] C. Monteserin, R. B. B. Barreiro, P. Vielva, E. Martinez-Gonzalez, M. P. Hobson and A. N. Lasenby, *A low CMB variance in the WMAP data*, *Mon. Not. Roy. Astron. Soc.* **387** (2008) 209 [0706.4289].

[99] M. Cruz, P. Vielva, E. Martinez-Gonzalez and R. B. Barreiro, *Anomalous variance in the WMAP data and Galactic Foreground residuals*, *Mon. Not. Roy. Astron. Soc.* **412** (2011) 2383 [1005.1264].

[100] A. Gruppuso, P. Natoli, F. Paci, F. Finelli, D. Molinari, A. De Rosa et al., *Low Variance at large scales of WMAP 9 year data*, *J. Cosmol. Astropart. P.* **1307** (2013) 047 [1304.5493].

[101] D. J. Schwarz, C. J. Copi, D. Huterer and G. D. Starkman, *CMB Anomalies after Planck*, *Class. Quant. Grav.* **33** (2016) 184001 [1510.07929].

[102] U. Natale, A. Gruppuso, D. Molinari and P. Natoli, *Is the lack of power anomaly in the CMB correlated with the orientation of the Galactic plane?*, *J. Cosmol. Astropart. P.* **1912** (2019) 052 [1908.10637].

[103] E. Dudas, N. Kitazawa, S. P. Patil and A. Sagnotti, *CMB Imprints of a Pre-Inflationary Climbing Phase*, *J. Cosmol. Astropart. P.* **1205** (2012) 012 [1202.6630].

[104] N. Kitazawa and A. Sagnotti, *Pre-inflationary clues from String Theory?*, *J. Cosmol. Astropart. P.* **1404** (2014) 017 [1402.1418].

[105] A. Gruppuso, N. Kitazawa, N. Mandolesi, P. Natoli and A. Sagnotti, *Pre-Inflationary Relics in the CMB?*, *Phys. Dark Univ.* **11** (2016) 68 [1508.00411].

[106] A. Gruppuso, N. Kitazawa, M. Lattanzi, N. Mandolesi, P. Natoli and A. Sagnotti, *The Evens and Odds of CMB Anomalies*, *Phys. Dark Univ.* **20** (2018) 49 [1712.03288].

[107] A. Gruppuso and A. Sagnotti, *Observational Hints of a Pre–Inflationary Scale?*, *Int. J. Mod. Phys.* **D24** (2015) 1544008 [1506.08093].

[108] S. M. Carroll, G. B. Field and R. Jackiw, *Limits on a Lorentz and Parity Violating Modification of Electrodynamics*, *Phys. Rev. D* **41** (1990) 1231.

[109] G.-C. Liu, S. Lee and K.-W. Ng, *Effect on cosmic microwave background polarization of coupling of quintessence to pseudoscalar formed from the electromagnetic field and its dual*, *Phys. Rev. Lett.* **97** (2006) 161303 [astro-ph/0606248].

[110] B. Feng, M. Li, J.-Q. Xia, X. Chen and X. Zhang, *Searching for CPT Violation with Cosmic Microwave Background Data from WMAP and BOOMERANG*, *Phys. Rev. Lett.* **96** (2006) 221302 [astro-ph/0601095].

[111] G. Gubitosi, L. Pagano, G. Amelino-Camelia, A. Melchiorri and A. Cooray, *A Constraint on Planck-scale Modifications to Electrodynamics with CMB polarization data*, *J. Cosmol. Astropart. P.* **0908** (2009) 021 [0904.3201].

[112] A. Gruppuso, M. Gerbino, P. Natoli, L. Pagano, N. Mandolesi, A. Melchiorri et al., *Constraints on cosmological birefringence from Planck and Bicep2/Keck data*, *J. Cosmol. Astropart. P.* **1606** (2016) 001 [1509.04157].

[113] A. Gruppuso, G. Maggio, D. Molinari and P. Natoli, *A note on the birefringence angle estimation in CMB data analysis*, *J. Cosmol. Astropart. P.* **1605** (2016) 020 [1604.05202].

[114] Planck Collaboration Int. XLIX, *Planck intermediate results. XLIX. Parity-violation constraints from polarization data*, *Astron. Astrophys.* **596** (2016) A110 [1605.08633].

[115] Y. Minami, H. Ochi, K. Ichiki, N. Katayama, E. Komatsu and T. Matsumura, *Simultaneous determination of the cosmic birefringence and miscalibrated polarization angles from CMB experiments*, *PTEP* **2019** (2019) 083E02 [1904.12440].

[116] Y. Minami, *Determination of miscalibrated polarization angles from observed CMB and foreground EB power spectra: Application to partial-sky observation*, *PTEP* **2020** (2020) 063E01 [2002.03572].

[117] H. Sugai, P. A. R. Ade, Y. Akiba, D. Alonso, K. Arnold, J. Aumont et al., *Updated Design of the CMB Polarization Experiment Satellite LiteBIRD*, *J. Low Temp. Phys.* (2020) [2001.01724].

[118] K. M. Górski, E. Hivon, A. J. Banday, B. D. Wandelt, F. K. Hansen, M. Reinecke et al., *HEALPix: A Framework for High-Resolution Discretization and Fast Analysis of Data Distributed on the Sphere*, *Astrophys. J.* **622** (2005) 759 [astro-ph/0409513].